Dynamic bonds and polar ejection force distribution explain kinetochore oscillations in PtK1 cells

Gul Civelekoglu-Scholey,[1] Bin He,[2] Muyao Shen,[2] Xiaohu Wan,[3] Emanuele Roscioli,[2] Brent Bowden,[2] and Daniela Cimini[2]

[1]Department of Molecular and Cellular Biology, University of California, Davis, CA 95616
[2]Department of Biological Sciences, Virginia Polytechnic Institute and State University, Blacksburg, VA 24061
[3]Department of Biology, University of North Carolina, Chapel Hill, NC 27599

Duplicated mitotic chromosomes aligned at the metaphase plate maintain dynamic attachments to spindle microtubules via their kinetochores, and multiple motor and nonmotor proteins cooperate to regulate their behavior. Depending on the system, sister chromatids may display either of two distinct behaviors, namely (1) the presence or (2) the absence of oscillations about the metaphase plate. Significantly, in PtK1 cells, in which chromosome behavior appears to be dependent on the position along the metaphase plate, both types of behavior are observed within the same spindle, but how and why these distinct behaviors are manifested is unclear. Here, we developed a new quantitative model to describe metaphase chromosome dynamics via kinetochore–microtubule interactions mediated by nonmotor viscoelastic linkages. Our model reproduces all the key features of metaphase sister kinetochore dynamics in PtK1 cells and suggests that differences in the distribution of polar ejection forces at the periphery and in the middle of PtK1 cell spindles underlie the observed dichotomy of chromosome behavior.

Introduction

One of the key steps in ensuring equal partitioning of the genome during mitosis is the alignment of mitotic chromosomes at the cell/spindle equator to form the so-called metaphase plate. Chromosome congression to the metaphase plate is favored by chromosome–microtubule [MT] interactions, and key players for these interactions include several molecular motors (e.g., CENP-E at kinetochores [KTs] and chromokinesins along chromosome arms), structural KT components (e.g., Ndc-80 complex), and MT dynamics (for reviews see McIntosh et al., 2002; Maiato et al., 2004). Once achieved, alignment at the metaphase plate must be maintained until the onset of anaphase, as anaphase in the presence of unaligned chromosomes would inevitably result in the formation of aneuploid daughter cells (for review see Cimini, 2008). Like chromosome congression to the metaphase plate, maintenance of alignment is believed to depend primarily on KT-associated motors (e.g., dynein, CENP-E), chromosome-associated motors (chromokinesins), biophysical properties of the KT–MT interface (e.g., compliance of Ndc-80 molecules), and regulators of MT dynamics (e.g., kinesin 13 and Aurora B kinase). Alignment at the spindle equator can be maintained when the forces that act on the chromosomes achieve a balance (Gardner and Odde, 2006; Vladimirou et al., 2011). However, despite maintenance of overall alignment at the metaphase plate, chromosomes are not necessarily static and the plus ends of KT-bound MTs (kMTs), and thus KT–MT attachments, remain dynamic during metaphase. In some cell types, including most animal tissue culture cells, fission yeast, and budding yeast, sister KT pairs at the metaphase plate oscillate back and forth (Funabiki et al., 1993; Skibbens et al., 1993; Pearson et al., 2001; Salic et al., 2004; Magidson et al., 2011), and the chromatin between sister KTs is stretched to levels significantly above rest length (Maddox et al., 2002; Jaqaman et al., 2010; Stumpff et al., 2011; Wan et al., 2012). In other systems, such as *Xenopus laevis* egg extracts, *Drosophila melanogaster* embryos, *Drosophila* S2 cells, insect

G. Civelekoglu-Scholey and B. He contributed equally to this paper.

Correspondence to Daniela Cimini: cimini@vt.edu; or Gul Civelekoglu-Scholey: egcivelekogluscholey@ucdavis.edu

Abbreviations used in this paper: AP, away-from-the-pole; DI, dynamic instability; FB, force–balance; kMT, kinetochore-bound microtubule; KT, kinetochore; MT, microtubule; ODE, ordinary differential equation; P movement, poleward movement; PEF, polar ejection force.

The Rockefeller University Press $30.00
J. Cell Biol. Vol. 201 No. 4 577–593
www.jcb.org/cgi/doi/10.1083/jcb.201301022

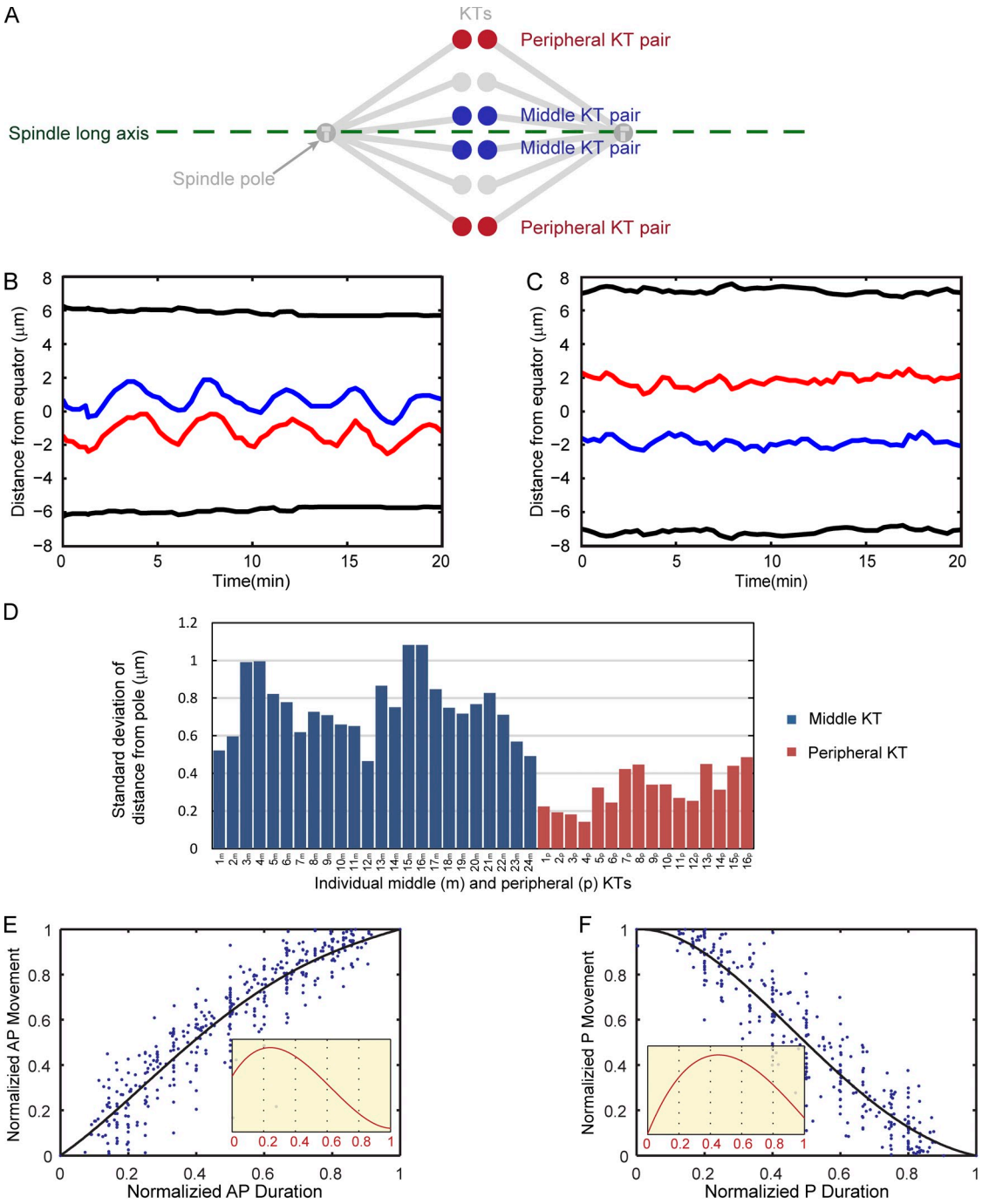

Figure 1. **Middle and peripheral sister KT pairs at the metaphase plate display significant differences in dynamics.** (A) Diagram illustrating how middle and peripheral KT pairs were defined with respect to the metaphase plate and the spindle long axis. In each cell analyzed, quantifications/measurements were performed for the two peripheral KT pairs (one on each side) and for two middle KT pairs, as illustrated in the diagram. (B and C) Representative examples of dynamics of middle (B) and peripheral (C) sister KT pairs in live metaphase PtK1 cells. (D) Distribution of the standard deviations of the distances from the pole for middle (blue) and peripheral (red) KTs. (E and F) Kinetic profiles of normalized P (F) and AP (E) movement for oscillating (middle) KTs. The solid lines through the kinetic data in E and F were obtained by fourth-degree polynomial fitting. The insets in E and F represent the normalized AP and P velocity kinetics obtained from the derivatives of the polynomial curves of AP and P movement, respectively. The data presented in this figure were obtained by analyzing 24 middle KT pairs and 16 peripheral KT pairs.

spermatocytes, oocytes, and higher plant cells, chromosomes do not exhibit oscillations (Desai et al., 1998; LaFountain et al., 2001; Brust-Mascher and Scholey, 2002; Maddox et al., 2002, 2003; de Lartigue et al., 2011), although their centromeres are under tension, as indicated by the stretching between the two sister KTs. Finally, one interesting example is represented by PtK1 cells, whose chromosomes have been reported to exhibit different behaviors depending on the position along the metaphase plate. Sister KT pairs positioned at the edges/periphery of the metaphase plate (as defined by the long axis of the metaphase plate) or farthest away from the spindle long axis (Fig. 1 A) do not oscillate, whereas chromosomes in the

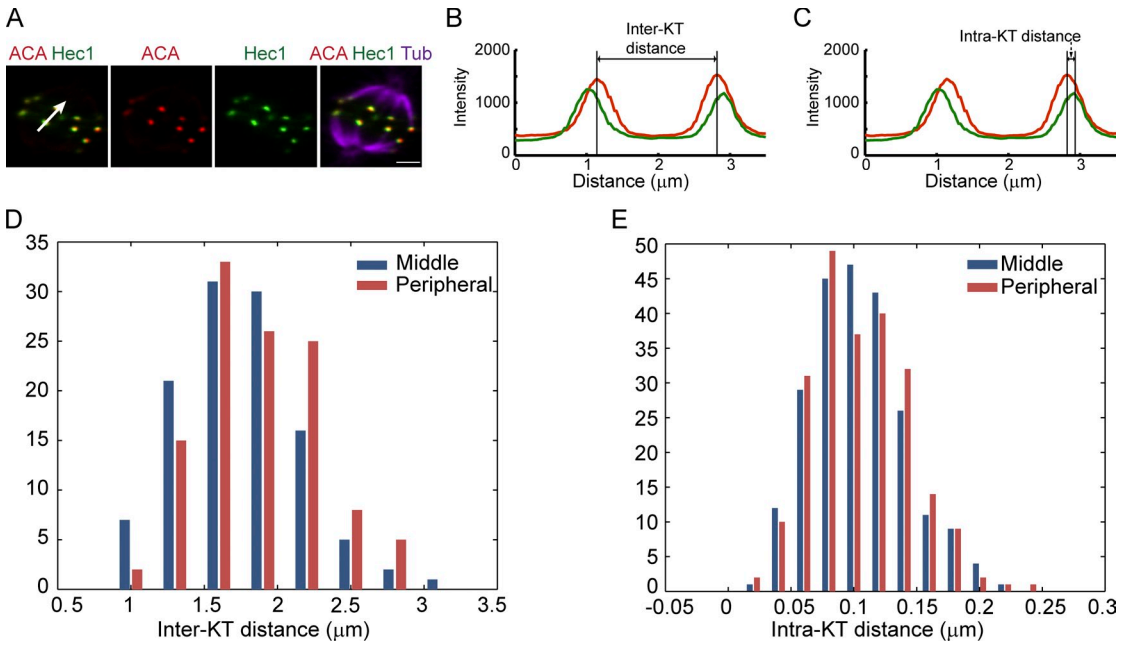

Figure 2. **Middle and peripheral KT pairs display similar inter- and intra-KT distances.** (A) Example of a metaphase PtK1 cell immunostained for α-tubulin (purple), ACA (red), and Hec1 (green). The white arrow in A indicates the position and direction of the line scan for the fluorescence intensity profiles displayed in B and C. Bar, 5 µm. (B and C) Fluorescence intensity profiles obtained from a line scan along the arrow traced in A. The inter- and intra-KT distances were obtained by measuring the distance between the ACA peaks (B) and the Hec1 and ACA peak (C), respectively. This method was used to measure the inter- and intra-KT distances in two pairs of middle sister KTs and two pairs of peripheral sister KTs in each of 57 cells. The data obtained from these measurements are reported in D and E. (D) Distribution of inter-KT distances in metaphase PtK1 cells (1.90 ± 0.44 µm and 2.01 ± 0.40 µm for middle and peripheral sister KTs; *n* = 57 cells). (E) Distribution of intra-KT distances in metaphase PtK1 cells (0.11 ± 0.04 µm for both middle and peripheral sister KTs; *n* = 57 cells).

middle of the metaphase plate or closer to the spindle long axis (Fig. 1 A) exhibit regular oscillations back and forth about the metaphase plate (Cimini et al., 2004; Cameron et al., 2006; Wan et al., 2012).

Pioneering quantitative studies have analyzed how various components of the force–balance (FB) network may affect chromosome congression and maintenance of alignment at the metaphase plate (for review see Vladimirou et al., 2011), and the dynamics of chromosome oscillation at the metaphase plate have been carefully characterized in various experimental systems (Skibbens et al., 1993; Pearson et al., 2001; Magidson et al., 2011). However, an investigation of the mechanisms responsible for differences in chromosome behavior within the same, unperturbed mitotic spindle is still lacking. Thus, we have used experimental data available for PtK1 cells to examine the dichotomy of chromosome oscillation at the metaphase plate in a quantitative framework. We have then validated this novel quantitative model by experimentally testing its predictions, thus attaining a detailed understanding of how the KT–MT interface modulates metaphase chromosome dynamics.

Results

Dynamics of metaphase chromosomes in PtK1 cells: oscillating and steady KT pairs

In PtK1 cells, KT pairs located in the middle and the periphery of the metaphase plate (Fig. 1 A) exhibit different dynamics. Although middle KT pairs undergo directional instability (oscillations between the poles; Skibbens et al., 1993; Fig. 1 B), the peripheral KT pairs (the two outermost KT pairs, one on each side of the metaphase plate) remain stably positioned near the spindle equator, and do not oscillate (Fig. 1 C). This is indicated by the large standard deviations for the distances between middle KTs and spindle poles (Fig. 1 D, blue) as opposed to much smaller standard deviations for the distances between peripheral KTs and spindle poles (Fig. 1 D, red). The characteristic regular oscillations displayed by middle KTs produced characteristic kinetic profiles of poleward (P) and away-from-the-pole (AP) movements (Fig. 1, E and F), as well as characteristic P and AP velocity profiles (Fig. 1, E and F, insets), which were consistent with previously reported data (Wan et al., 2012). Such profiles could not be obtained for peripheral KTs, as they only exhibited small (<1 µm in amplitude) erratic movements (Fig. 1, C and D). Despite the differences in oscillations, the intra-KT distances for middle KT pairs did not differ from those observed for peripheral KT pairs (*t* test, P = 0.73), whereas the inter-KT distances only displayed slight differences (*t* test, P = 0.05; Fig. 2).

FB model for metaphase chromosome dynamics in PtK1 cells

To investigate the mechanism underlying chromosome alignment and dynamics in PtK1 cells, we modified the FB model initially developed to describe chromosome dynamics in the *Drosophila* embryo (Civelekoglu-Scholey et al., 2006) and adapted it to PtK1 cell metaphase chromosome dynamics by appropriately changing the model parameters (e.g., the number of MT attachment sites at the KT, MT dynamic instability (DI)

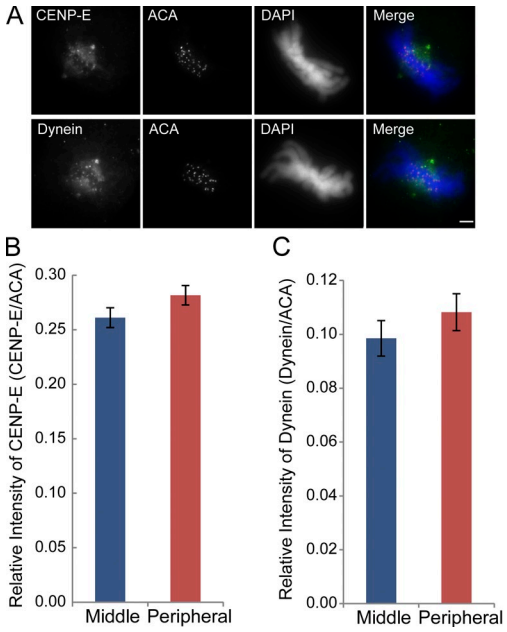

Figure 3. **Similar amounts of KT motors (CENP-E and dynein) accumulate at middle and peripheral KTs.** (A) Examples of metaphase PtK1 cells immunostained for CENP-E (top, first column) or dynein (bottom, first column) and ACA (second column). The chromosomes were stained with DAPI. In the merged images, DAPI is shown in blue, ACA in red, and the motors in green. Bar, 5 µm. (B and C) Quantification of CENP-E (B) and dynein (C) at the KTs of middle versus peripheral KTs (n = 46 cells) Error bars indicate mean ± SEM.

parameters, velocity of poleward sliding motors), including a force-dependent detachment behavior of the KT (dynein and Cenp-E) and sliding motors, and assuming that the cohesin bonds between sister chromatids have viscoelastic properties (Fig. S1, A–C; and Materials and methods). In this model, the sliding motors on the kMTs generate poleward-directed pulling/sliding forces (according to their force–velocity relationship), and it is simply assumed that the kMT minus ends at the spindle poles are depolymerized at the rate the kMTs slide into the poles. Thus, because in the model the sliding rate is equivalent to the kMT poleward flux rate, "sliding" and "flux" will be used interchangeably hereafter. The revised model accounted for many of the quantified aspects of the PtK1 chromosome dynamics, including the number of kMTs, the slow flux rates and MT dynamics, and their oscillation around the metaphase plate (Fig. S1, D and E), but did not reproduce the inter-KT oscillations: i.e., oscillations in the distance between a pair of sister KTs. Indeed, it has been recently reported that during metaphase, although sister KTs oscillate between the spindle poles with period τ (where τ is the duration of a full cycle, or the time it takes for a P-moving KT to return to the same position in a P-moving state), the distance between sister KTs oscillates with a period equal to half of that, i.e., $\tau/2$ (Wan et al., 2012).

We then tried to identify the possible mechanisms that could account for the observed differences in behavior between middle and peripheral chromosomes by varying the model parameters (e.g., the number of motors per KT, polar ejection forces [PEFs], cohesin force). The model predicts that, with the same MT dynamic parameters and MT flux rates, different behavior of the middle and peripheral KT pairs (oscillatory vs. steady) can be produced only if (a) there are higher PEFs at the spindle periphery compared with the middle of the spindle or (b) there are imbalances in the numbers of motors (dynein or CENP-E) at the peripheral versus middle KTs. Because in Ptk1 cells the largest chromosomes are always positioned at the periphery of the metaphase plate (Torosantucci et al., 2009), it is reasonable to think that the larger surface area of MT–chromosome interaction may result in higher PEFs. However, when we introduced higher peripheral PEFs, the model also predicted a reduction of the inter-KT stretch, which was inconsistent with the experimental data. Lower numbers of CENP-E or higher numbers of dynein at the peripheral KTs did not suppress oscillations and resulted in increased inter-KT distances, whereas higher numbers of CENP-E or lower numbers of dynein at the peripheral KTs suppressed oscillations, but also induced a reduction in inter-KT stretching, which is inconsistent with the experimental data. Moreover, quantification of KT-associated CENP-E and dynein did not reveal any difference between peripheral and middle KT pairs (Fig. 3). Thus, differences in the number of KT-associated motors could not explain the dichotomy of behavior between the middle and peripheral sister KT pairs, which suggests that, unlike in the fast *Drosophila* syncytial embryo mitosis (Bader and Vaughan, 2010), the KT motors CENP-E and dynein do not play a major role in regulating metaphase chromosome dynamics in PtK1 cells.

New mathematical model: KT attachment to MTs through dynamic nonmotor, viscoelastic bonds

Recent in vivo and in vitro studies have suggested a key role of nonmotor linkages between MTs and KTs in yeast and tissue culture cells (McIntosh et al., 2008; Joglekar and DeLuca, 2009; Powers et al., 2009; Akiyoshi et al., 2010; Asbury et al., 2011). Based on these studies and the observation that MT-attached KTs undergo intra-KT deformations (Maresca and Salmon, 2009; Uchida et al., 2009; Dumont et al., 2012), we revised our FB model for chromosome motility to explore if dynamic nonmotor, viscoelastic bonds between MTs and KTs could account for the observed behavior of metaphase chromosomes in PtK1 cells. It is important to specify that the assumption that both the KT–MT bonds and the cohesin bonds have viscoelastic, instead of simply elastic, properties is essential to produce smooth rather than jerky KT movements, and ensures that the KT oscillations as well as the changes in intra-KT distances are smooth and similar to the dynamic behavior observed experimentally. Based on these assumptions, we considered viscoelastic dynamic linkages between the dynamic MT plus ends and the KTs, in the absence of MT-based motors (Fig. 4, A–C). Within this minimal FB approach, we wished (a) to address the question of whether dynamic viscoelastic attachments of the sister KTs to multiple and dynamic MT plus ends provide a robust attachment of metaphase sister KTs to MTs undergoing poleward flux; (b) to quantitatively address whether force-sensitive stochastic attachment/detachment of viscoelastic linkages coupled to MT poleward sliding/flux is sufficient to account for the experimentally observed chromosome behavior;

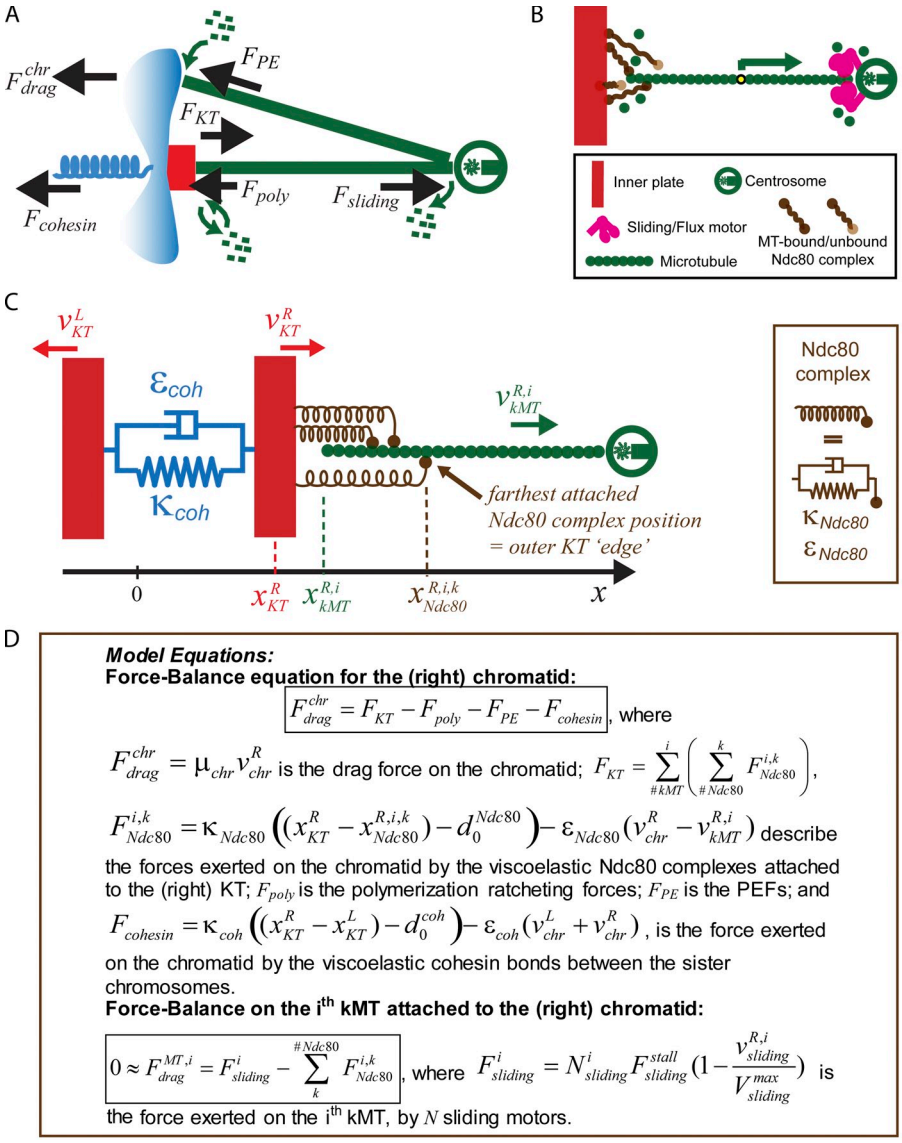

Figure 4. **FB model description.** (A) Forces exerted on a (right) sister KT and a single kMT (note, each KT binds a bundle of kMTs, or k-fiber). (B) Close-up of the KT–MT interface and the viscoelastic Ndc80 complexes. (C) Mechanical properties of cohesin and Ndc80 complexes and positions of the kMT plus end, the KTs, and the Ndc80 bonds along the pole–pole axis. (D) Model equations.

(c) to identify which components, or properties of the components in the FB model (by inference, the molecules in the spindle), are at the core of the observed metaphase chromosome oscillations; and (d) to investigate which geometric property of, or inhomogeneity in, the spindle/chromosomes could govern the dichotomy in the behavior of metaphase sister KT pairs within the PtK1 spindle.

Our new FB model describes the dynamics of sister KT pairs, which interact, via viscoelastic linkages, with multiple MTs that undergo DI at their plus ends and slide poleward and depolymerize at their minus ends. It is worth noting that the viscoelastic linkages in our model could depend on the viscoelastic properties of any or all of the components of the KNL1–Mis12 complex–Ndc80 complex (KMN) network (Cheeseman and Desai, 2008) at the outer KT. However, because the Ndc80 complex has been shown to be the KMN subcomplex that directly binds MTs (Cheeseman et al., 2006; DeLuca et al., 2006), we will refer to the Ndc80 complex as the key element in the KT–MT viscoelastic linkages of our model. In the model, the velocities of the sister KTs and the poleward flux/sliding velocities of the kMTs are dependent on the sum of the poleward and antipoleward forces exerted on them by the cohesin links between the sister KTs, the bound Ndc80 complexes, the force exerted on the kMTs by the poleward flux motors/depolymerases "reeling in" or "sliding" the MTs poleward, and the viscous drag on the KTs and the MTs (Fig. 4). In the absence of forces generated by poleward-directed motors at the KT, the sole poleward force generators/transducers at the KT are the bound and stretched Ndc80 complexes. At a given time, different Ndc80 complexes anchored to the same kMT may exert forces of different magnitude, reflecting their current stretch/compression as a result of their uncoordinated stochastic attachment/detachment events. In the model, we assume that the binding rates of the Ndc80 complex to polymerizing or depolymerizing MTs are the same, but the detachment rates from polymerizing or depolymerizing MTs differ. Namely, we assume that the detachment of the Ndc80 complexes from depolymerizing MTs occurs in a biphasic, force-sensitive manner (it is high at low force, decreases at moderate force, then increases again under high force), whereas the detachment rate from polymerizing MT tips increases linearly

Table 1. **Model assumptions**

Core assumptions	Added assumptions	Assumptions vital for model's robustness
KTs attach to MTs through dynamic, viscoelastic, nonmotor linkages (Ndc80 complexes)	Ndc80 complexes have different detachment kinetics for polymerizing/depolymerizing (GTP/GDP-tubulin) tips of MTs	An MT plus end cannot depolymerize past an Ndc80 complex attachment position
When bound to a MT, each extended/compressed Ndc80 complex exerts a force (e.g., poleward/anti-poleward) on its KT, and reciprocally to the MT to which it is bound	Ndc80 complexes behave as tension sensors (force-dependent kinetics)	Detachment of Ndc80 complex from polymerizing and depolymerizing MTs differs, both in the absence and the presence of tension force
Ndc80 complexes bind to and detach from MTs independently from one another	MT plus end catastrophe rate is length-dependent	Ndc80 complex binds "weakly" to polymerizing and, in a biphasic way, "strongly" to depolymerizing MTs under moderate force
Cohesin bonds between sister KTs behave as viscoelastic material	KT-bound MT plus-end catastrophe rate is growth rate–dependent (increases with decreasing growth rate)	
Both KT-bound and free MT plus ends undergo DI	KT-bound MT plus end rescue rate is regulated by tension forces exerted on it by the Ndc80 complexes (increased rescue under high tension)	
A polymerizing MT plus end stalls when it reaches the inner KT		
MT minus ends slide polewards by sliding/flux motors and depolymerize at the rate the MTs are slid into the poles		

with force (see Materials and methods; Fig. 4 D, Fig. S2, and Table 1). In this minimal model, we do not account for additional poleward pulling forces that may stem from the power stroke/curling out of depolymerizing protofilaments (Grishchuk et al., 2005; Asbury et al., 2011) to which the Ndc80 complexes may be attached. We do not account for polymerization ratcheting forces at the inner-KT plate either, and simply assume that MT polymerization at the plus end stalls at a critical distance from the inner-KT plate. The specific assumptions of the model are summarized in Table 1. The model was initially constructed with a minimal set of assumptions (Table 1, first column), and the assumption set was gradually augmented (Table 1, second and third column), until the model reproduced the experimentally observed behavior of metaphase sister KT pairs. Based on the core equations in Fig. 4 D, a large set of coupled FB model equations (typically 52–102 equations, ranging from 25–50 kMT for each of the two sister KTs) was constructed. These equations were then solved numerically using a custom-made MATLAB script in an iterative process (see Materials and methods for details).

Model results: robust attachment of KTs to spindle MTs, and oscillations of middle sister KT pairs

The minimal model described in the previous section faithfully reproduces the metaphase oscillations of sister KTs (in amplitude and period) and the inter-KT distance observed in PtK1 cells (Fig. 5, A–C), including the recently documented period doubling in inter-KT distance for oscillating KT pairs (Dumont et al., 2012; Wan et al., 2012; Fig. 5 A, green trace). The model also accounts well for several experimental observations, including inter- and intra-KT distance distributions (Figs. 5, C and D, respectively) for the oscillating sister KT pairs, the mean number and the evolution of the number of bound kMTs (Fig. 5 E and Video 1; VandenBeldt et al., 2006), and MT poleward flux rates (Cameron et al., 2006). In addition, the time evolution of the numbers of attached MTs and that of the bound Ndc80 complexes corresponding to the P- and AP-moving sister KTs (Fig. 5, E and F) provide insight into the KT change in direction from P to AP movement during oscillations, illustrating that it is the number of bound Ndc80 complexes and not the number of MTs that determines the switch (Video 1). Furthermore, the differences in the mean and maximal intra-KT stretch (i.e., the distance between the inner KT and the mean position of the MT-bound Ndc80 complexes, and the distance between the inner KT and the farthest attached Ndc80 complex, respectively) for the P- and AP-moving sister KT (Fig. 4 C), show that the maximal intra-KT stretch matches the recently documented data for PtK2 cells where the AP-moving sister was found to exhibit higher intra-KT stretch (Dumont et al., 2012; Fig. 5, G and H). Finally, the model can reproduce the experimentally observed P and AP kinetics (compare Fig. 5, I and J; and Fig. 1, E and F; Wan et al., 2012). Both the model and the experimental data also show that the AP-moving KT reaches its maximum speed earlier than the P-moving KT (Fig. 5, I and J; and Fig. 1, E and F, insets; Wan et al., 2012). In fact, these differences in acquisition of the maximal speed during P and AP movement are responsible for the observed period doubling in the inter-KT distance (Dumont et al., 2012; Wan et al., 2012; Fig. 5 A). Our model suggests that this is due to the biphasic kinetics of the Ndc80 bonds attached to depolymerizing MTs, resulting in a slower turnover of the kMT bonds of the P-moving sister (under moderate tension), hindering the increase in P velocity until a critical tension level is reached. The proposed biphasic dissociation kinetics of Ndc80 complexes are not a general property of molecular motors and may underlie how different organisms use and rely on motor or nonmotor proteins for chromosome alignment and dynamics.

The positive feedback, which results in sister KT oscillations about the metaphase plate, and the phase difference between

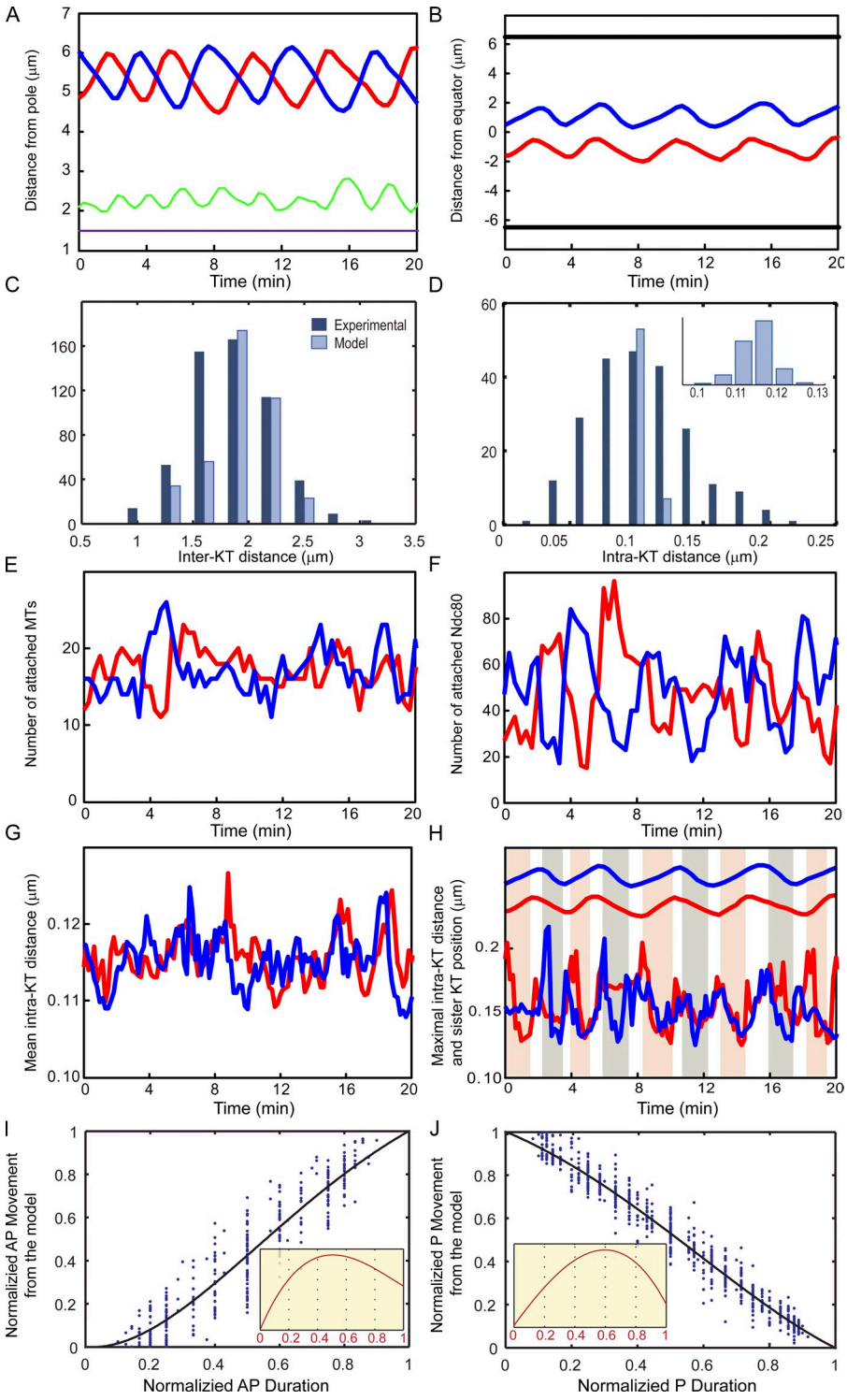

Figure 5. **A model based on dynamic viscoelastic KT–MT bonds reproduces the dynamic behavior of middle sister KT pairs.** (A) KT–pole (left KT, red; right KT, blue) and inter-KT (green) distances, and cohesin rest length (purple) over time. The periods of sister KT and inter-KT oscillations (by fast Fourier transform) are 280 s and ~5 min and 150 s and ~2.5 min, respectively (compare with Fig. 1 B). (B) Position of sister KTs (left KT in red, right KT in blue) and spindle poles (black) over time (the spindle equator is set to zero). (C and D) Inter- (C) and intra-KT (D) distances produced by the model (2.31 ± 0.24 μm [n = 400] and 0.12 ± 0.01 μm [n = 60], respectively) shown side-by-side with the distance observed experimentally in live (inter-KT distances; n = 558) or fixed (intra-KT distances; n = 228) cells. Experimental data are shown in dark blue and model data are shown in light blue. The inset in D shows a close-up of the distribution of the data produced by the model. (E–H) Time evolution of the total number of attached MTs (17 ± 4 and 44% in depolymerization state; E), attached Ndc80 complexes (49 ± 19; F), and mean (G) and maximal (H) intra-KT distance of the left (red) and right (blue) sister KTs. In H, the maximum intra-KT distances and the corresponding sister KT positions for the left (red) and right (blue) sister KTs are shown over time. The gray and pink shaded areas mark the AP movement of the sister attached to the right and left pole, respectively. The AP-moving sister generally displays a higher intra-KT distance. (I and J) Kinetic profiles of normalized P (J) and AP (I) movement for oscillating KTs. The solid lines through the kinetic data in I and J were obtained by fourth-degree polynomial fitting. The insets in I and J represent the normalized AP and P velocity kinetics obtained from the derivatives of the polynomial curves of AP and P movement, respectively. Note, the slight differences between the model and the experimental results (I and J vs. Fig. 1, E and F, insets) can be explained by the fact that the time of the P-AP switch can be tracked with high precision in the model, but not in the experiments. This would account for the delay in the normalized time for reaching maximal velocity for both the AP- and P-moving sister KTs in the model results. An example of a model simulation of KT and kMT dynamics for an oscillating middle KT pair is shown in Video 1 (top).

the oscillatory behavior of the sister KTs causing the period-doubling of the inter-KT distance oscillations, can be understood as follows. At the spindle equator, the sister KTs initially have no advantage over one another in terms of forces, and their Ndc80 complex–MT bonds turn over with similar dynamics as they attach to MTs, stretch, and detach. However, when a KT stochastically acquires attachment to a higher ratio of depolymerizing/polymerizing MTs compared with its sister KT, and begins moving poleward slowly, it gains an advantage in "bond stability" for its depolymerizing kMTs. This is due to the biphasic force sensitivity of the detachment kinetics: at moderate tension, the Ndc80 bonds with depolymerizing MTs are stabilized (k_{off} is low), whereas those with low or high tension turnover rapidly. Furthermore, the P movement enhances the catastrophe frequency of polymerizing kMT plus ends, thus increasing the ratio of depolymerizing/polymerizing MTs further, and at the same time increasing the P movement rate of the KT, which relieves the tension on the Ndc80 complexes, allowing them to

Table 2. **Model test for suppression of KT oscillations**

Tested condition	Suppression of KT oscillations	Additional observed changes
Higher kMT No. per KT	No	Increased inter-KT distance and oscillation amplitude
Angular projection of sliding force (45°)	No	Increased inter-KT distance
Higher chromosome viscous drag coefficient	No	Decreased oscillation amplitude and period
Higher/lower f_{cat}	No/no	Increased/decreased oscillation amplitude and period
Higher/lower PEF (linear)	Yes	Significantly reduced/increased inter-KT distance
Sharply increasing PEF (nonlinear)	Yes	None

turn over for effective motility. When the sister KT begins its P movement, its sister KT may also initially take (smaller) poleward steps, but it quickly stalls, then begins AP movement due to increasing cohesin forces. As the AP-moving sister gains speed due to increasing cohesin pulling forces, the Ndc80-bound depolymerizing MTs either lose their attachment due to high tension (the biphasic force dependence) or switch to polymerization due to increased rescue frequency, enhancing the AP sister's disadvantage in the ratio of depolymerizing/polymerizing kMTs. As the P-moving KT approaches its pole, the PEFs slow down its movement, elevating the Ndc80 tension again, and either causing the Ndc80 complexes to detach from depolymerizing MTs or leading to a rescue event of the kMT plus ends, shifting the advantage to the sister KT.

A highly attractive feature of this minimal model is the robustness of the KT–MT attachments to changes in the model parameters. For example, changing (within a reasonable range, see Table S1) the number of MT attachment sites per KT, the number of Ndc80 complexes per MT, or the MT plus end dynamic rates does not compromise faithful attachment of the KT to spindle MTs, and the qualitative aspects of chromosome dynamics are not affected. However, to reproduce certain specific aspects of chromosome dynamics observed experimentally, such as the period of inter- and intra-KT oscillations and the kMT number and poleward flux rates, fine-tuning of the parameters is required.

Model results: identification of parameters that suppress oscillations of the peripheral KT pairs

Next, we tested the model to identify changes in the parameters that could account for the observed behavior of the peripheral sister KT pairs (Cimini et al., 2004; Cameron et al., 2006; Wan et al., 2012), characterized by small (<1 µm in amplitude) erratic movements and lack of oscillations (Fig. 1 C). We tested several conditions, including differences in the number of kMTs per KT, PEFs, and MT sliding forces due to the geometry of the spindle (in these fairly flat mitotic PtK1 cells, the mean angle between the k-fiber and the peripheral KTs is 35°, in contrast with a mean angle of 90° for the middle KTs), differences in the catastrophe rate for the MT plus ends bound to the peripheral KTs (peripheral KTs have longer kMTs due to the geometry of the spindle and their position), and some combinations of the above possibilities (some shown in Table 2). We found that only a nonlinear distribution of the PEFs characterized by a sharp increase at short distance from the spindle equator (see Materials and methods; Fig. 6 A) led to the suppression of oscillations and at the same time produced inter- and intra-KT distances that matched the experimental data (Table 2; Fig. 6, B–E; and Video 1; see also Fig. 6, F and G; and Video 1 for evolution of the number of MTs and Ndc80 complexes). Indeed, simply decreasing the magnitude of the PEFs while maintaining a linear increase around the metaphase plate was not sufficient, as under these conditions oscillations were suppressed (as in Stumpff et al., 2012), but the inter-KT distances were significantly higher than those observed experimentally. Thus, we propose that the distribution of PEFs differs in the middle and the periphery of the spindle in PtK1 cells, and this governs the observed dichotomy in behavior of middle and peripheral KT pairs. Specifically, our model suggests that although PEFs increase linearly around the spindle equator for middle KTs, they increase sharply for the peripheral KTs (Fig. 6 A). This finding is consistent with laser ablation studies in which reduced PEFs resulted in increased amplitude of oscillations (Ke et al., 2009).

Model predictions and experimental tests

Our model makes several testable predictions (a–d below), some of which are supported by recently published work and some others that have been experimentally tested here.

(a) As the sister KTs begin their excursion, the fraction of kMTs in depolymerization/polymerization state for the P-moving chromosome initially increases, then decreases, while that of the AP-moving sister initially diminishes rapidly, then remains constant (low) until turnaround.

(b) Both the average and the maximal intra-KT distance oscillate. Specifically, the maximal intra-KT stretch of the AP-moving sister KT is, on average, larger than that of the P-moving chromosome, and it oscillates with a period roughly twice that of the sister KT oscillations about the metaphase plate (Fig. 5, G and H). Recent work by Dumont et al. (2012) in PtK cells showed that, indeed, the intra-KT stretch for P- and AP-moving KTs is different (intra-KT distance for P-moving KT was smaller than for AP-moving KT), providing support to our model results.

(c) When the detachment rate of the Ndc80 complex from MTs is inhibited, the sister KTs become hyperstretched (DeLuca et al., 2006; Fig. 7, A and C) solely due to the poleward sliding/flux of kMTs bound to the sister KTs. Therefore, coinhibition of poleward flux will reduce the inter-KT stretch (Fig. 7, C and D), but maintain fully attached (thick k-fibers) sister KTs. To test this prediction, we performed microinjection experiments with antibodies to the N terminus of Hec1 (as in DeLuca et al., 2006) and/or Kif2a (provided by D. Compton, Geisel School of Medicine at Dartmouth, Hanover, NH), which is believed to be the major depolymerase at the spindle poles responsible for MT poleward flux (Ganem et al., 2005; Ganem and Compton, 2006). Indeed, pilot experiments showed that injection of Kif2a antibodies in PtK1 cells significantly reduced poleward flux of kMTs

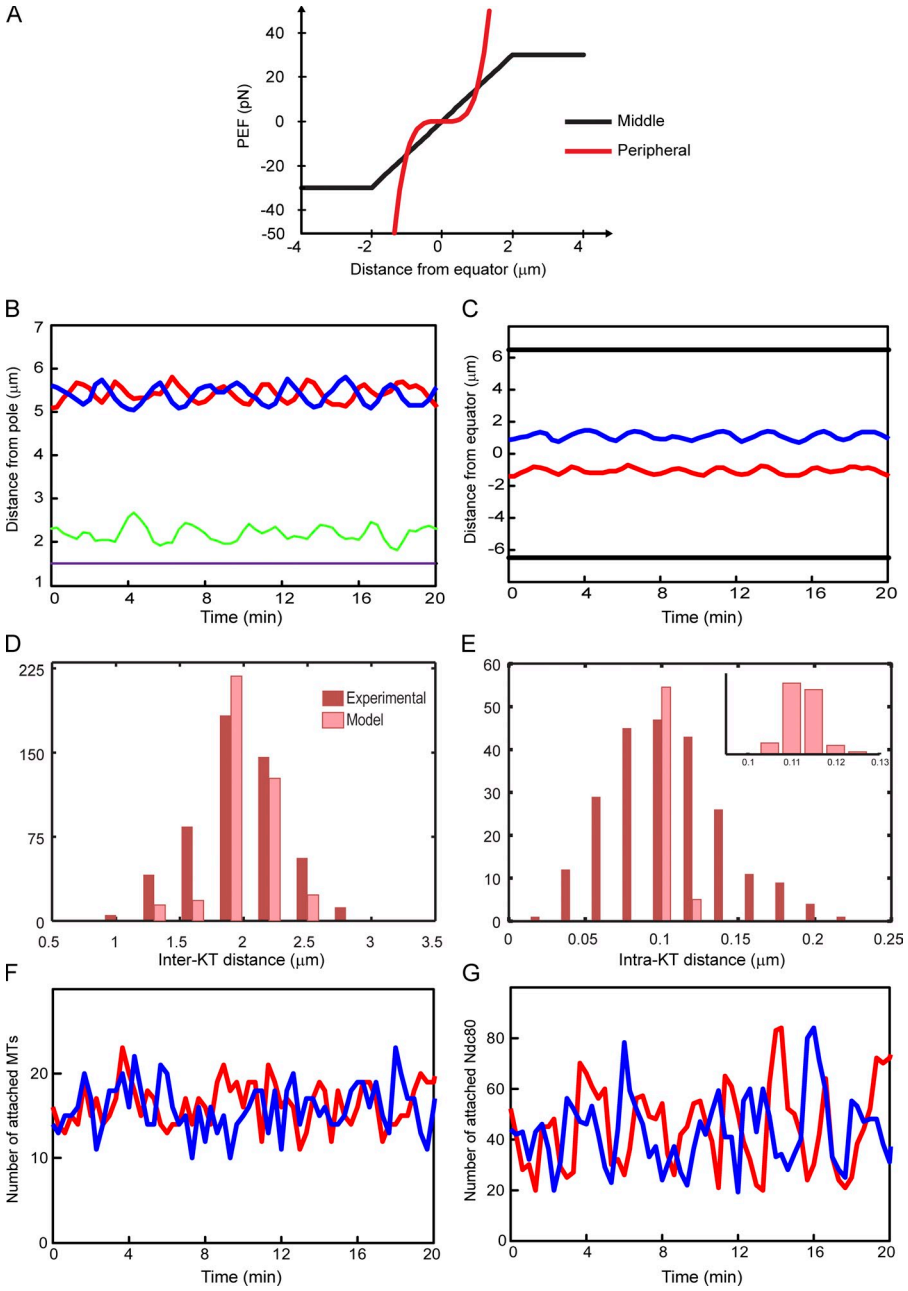

Figure 6. **A nonlinear distribution of PEFs can suppress the oscillations of peripheral sister KT pairs.** (A) Distribution of PEFs in the spindle: for KT pairs in the middle of the spindle, the PEFs initially decrease linearly away from the equator then stay constant toward the poles (black line). In contrast, for KT pairs at the periphery of the spindle, the PEFs are very low near the equator, then increase sharply (nonlinear) to high levels (red line). See Materials and methods for additional quantitative details. (B) KT–pole (left KT, red; right KT, blue) and inter-KT distance (green), and cohesin rest length (purple) over time. Note the erratic dynamic behavior. (C) Position of sister KTs (left KT in red, right KT in blue) and spindle poles (black) over time, compare with Fig. 1 B. (D and E) Inter- (D) and intra-KT (E) distances produced by the model (2.22 ± 0.16 μm [n = 400] and 0.12 ± 0.01 μm [n = 60], respectively) shown side-by-side with the distances observed experimentally in live (inter-KT distances, n = 530) or fixed (intra-KT distances, n = 228) cells. Experimental data are shown in dark red and model data are shown in light red. The inset in E shows a close-up of the distribution of the data produced by the model. (F and G) Time evolution of the total number of attached MTs (16 ± 3 and 42% in depolymerization state; F) and the total number of attached Ndc80 complexes (44 ± 16; G) for the left (red) and right (blue) sister KTs. An example of a model simulation of KT and kMT dynamics for a nonoscillating peripheral KT pair is shown in Video 1 (bottom).

(unpublished data). Such reduction in MT poleward flux produced a decrease in the inter-KT distance compared with uninjected cells (Figs. 7, E, F, I, J, M, and N; and Video 2), as predicted by our model (Fig. 7, A and B). Injection of Hec1 antibodies, however, induced a significant increase in inter-KT stretching (Fig. 7, G, K, and O; compared with Fig. 7, E, I, and M; and Video 2), which supports our model prediction (Fig. 7, C and A) and confirms previous observations (DeLuca et al., 2006). Importantly, when we coinjected Hec1 and Kif2a antibodies, we observed a significant reduction of inter-KT stretching (Fig. 7, H, L, and P; and Video 2) as compared with injection of the Hec1 antibody alone (Fig. 7, G, K, and O; and Video 2), once again supporting our model predictions (Fig. 7, C and D).

(d) Forces generated by poleward flux motors on spindle MTs coupled to dynamics of MT plus ends at the KT are sufficient to generate the experimentally observed inter- and intra-KT stretching. Indeed, simulations in which the poleward flux was reduced produced a reduction in inter-KT stretch (Fig. 7 B) compared with controls (Fig. 7 A). This prediction was supported by our experimental observation of reduced inter-KT stretch in cells microinjected with Kif2a antibodies (Fig. 7, F, J, and N; compared with Fig. 7, E, I, and M; and Video 2).

Discussion

The data presented here highlight how differences in the distribution of PEFs can affect metaphase chromosome oscillations, and suggest that biphasic, force-dependent detachment kinetics of Ndc80 complexes can drive the inter-KT distance oscillations

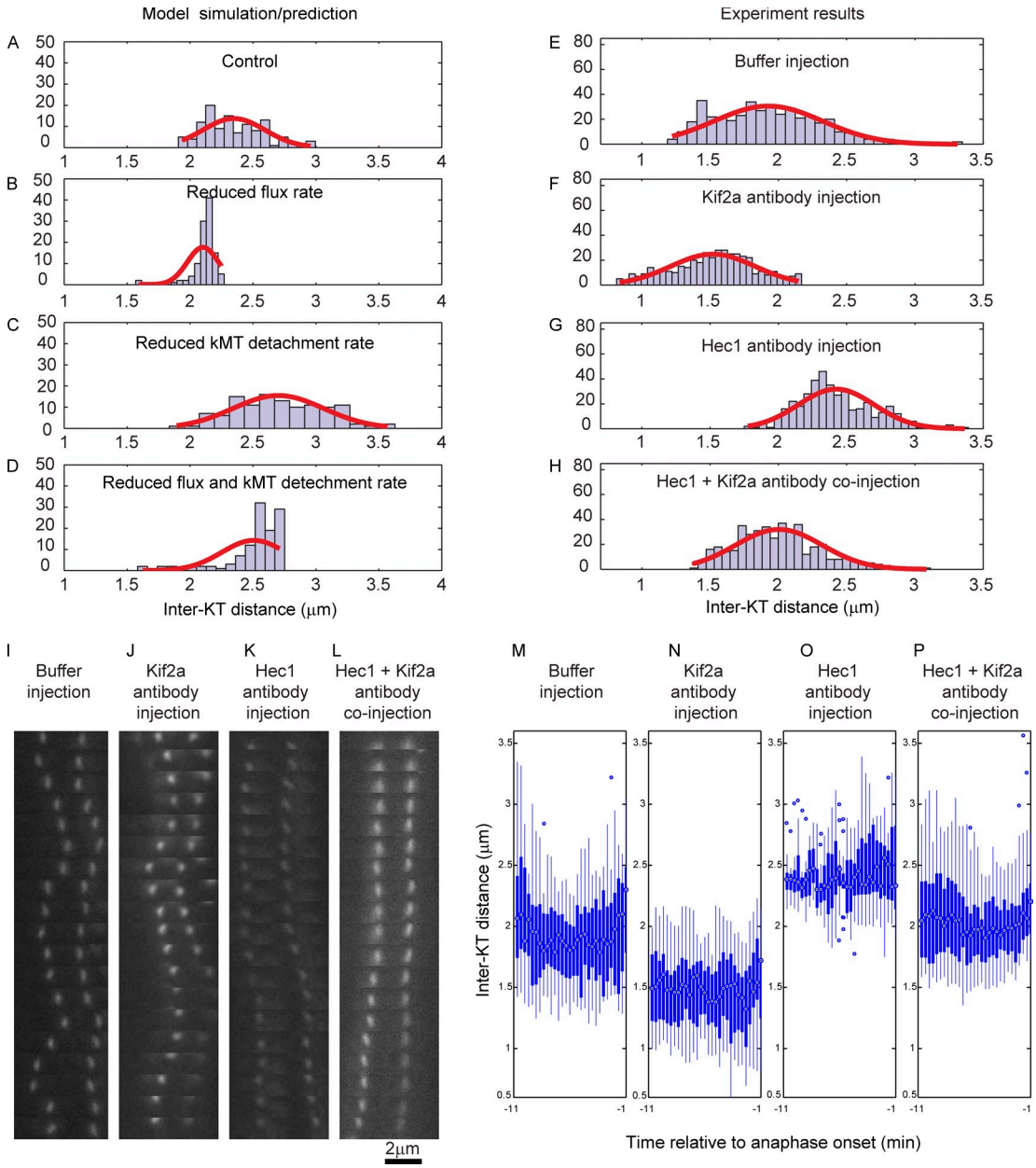

Figure 7. **Inter-KT hyperstretching caused by reduced kMT detachment rates can be rescued by simultaneous reduction of MT poleward flux.** (A–D) Model simulation results of the distribution of inter-KT distances under different conditions (n = 4 KT pairs in all cases). (E–H) Experimentally determined distribution of the inter-KT distances under different conditions. Reduction of MT poleward flux was achieved by microinjection of anti-Kif2a antibodies (F, n = 12 KT pairs); reduction of kMT detachment rate was achieved by microinjection of anti-Hec1 antibodies (G, n = 7 KT pairs); simultaneous reduction of MT poleward flux and kMT detachment rate was achieved by coinjection of the two antibodies (H, n = 12 KT pairs); HEK buffer injection (E, n = 8 KT pairs) was used as a control. (I–L) Time series of 19 frames (acquired at 20-s intervals) displaying individual KT pairs from videos of HEC1-GFP PtK1 cells microinjected as indicated in the figure labels. The last frame in each series represents anaphase onset. (M–P) Box plots of inter-KT distances in cells microinjected as indicated in the figure labels. Each dot in the graphs represents the median value of inter-KT distances obtained for different KT pairs (n = 8, 12, 7, and 12 KT pairs for M, N, O, and P, respectively) from 4–7 cells at the same time point; the boxes represent the 25th-75th percentile range; the whiskers extend to the most extreme data points not considered outliers. All the graphs display data for a 10-min interval preceding anaphase (up to 1 min before anaphase onset). Examples of microinjected cells can be viewed in Video 2.

observed in metaphase for oscillating sister KT pairs. Instead, the length- and polymerization rate–dependent catastrophe frequency, and the tension-dependent rescue frequency of MT plus ends, play more subtle roles by coordinating the dynamics of the plus ends of MTs attached to sister KTs to achieve efficient motility and, together with the viscoelasticity of cohesin and Ndc80 complexes, contribute to the smoothing out of the otherwise jerky chromosome movements.

What causes the inhomogeneity in the distribution of PEFs within the PtK1 cells' metaphase spindle?

We found that a difference in the distribution of the PEFs at the periphery versus the middle of the spindle can explain the differences in oscillations between peripheral and middle KT pairs in PtK1 cells. The predicted difference between the PEFs exerted on middle versus peripheral KTs can be explained by

several specific features of PtK1 mitotic cells: (a) the chromosomes aligned at the periphery of the metaphase plate always correspond to the two chromosomes 1 (Torosantucci et al., 2009), which are large acrocentric chromosomes, with a very long q arm (Torosantucci et al., 2009). Such large arm size results in high baseline PEF magnitude for peripheral KTs (see Materials and methods for further details). (b) Chromosomes at the periphery are fully exposed to non-KT MTs, whereas middle chromosomes are partly shielded due to the crowding in the middle of the metaphase plate, where each chromosome is surrounded by other chromosomes. (c) Because the KT-to-pole distance is greater for peripheral KTs, the length-dependent catastrophe frequency of MT plus ends (Varga et al., 2009) gives rise to a sharp drop in PEFs in close proximity to the spindle equator. Thus, the peripheral chromosome arms are exposed to low PEFs within a narrow region right around the spindle equator, but are exposed to sharply increasing PEFs as soon as they move away from the equator (Fig. 4 A).

One could argue that other forces arising from the great "crowding" within the mitotic spindle may affect the dynamics of metaphase chromosome behavior. For instance, forces exerted by chromosome arms bumping into one another, the inability of MTs to interact with all chromosomes in the same manner, and elastic MT forces exerted on the chromosomes are additional (stochastic) factors that are not considered in our model. However, the experimentally observed regularity of the middle sister KT oscillations suggests that the sum of these forces are of negligible magnitude compared with the forces that drive KT movements. In fact, the "crowded" organization of the spindle would also cause chromosome arms to shield their neighboring chromosomes from spindle MTs, particularly in the context of the middle KTs. We suggest that this would contribute significantly to the proposed differences in the PEFs for the middle and peripheral sister KTs, yielding a sharp increase of the PEFs around the spindle equator for the peripheral sister KTs, with no neighbors, and a linear increase in PEFs around the spindle equator for the middle sister KTs, with many neighbors. Thus, the averaged sum of forces due to crowding is implicitly included in our current model via the PEF profiles for the middle and the peripheral sister KTs (Fig. 6 A).

Comparison with previous models

The model developed and presented here is closely related to the model developed by Joglekar and Hunt (2002) for PtK1 chromosome dynamics, where the authors investigated the Hill-sleeve model (Hill, 1985) in an FB approach. Our model differs from theirs in the following ways: first, the Joglekar and Hunt (2002) model did not consider poleward flux of kMTs. Next, in the Joglekar-Hunt model the attachment sites of KTs to each MT are arranged in series in form of a "sleeve," with multiple sleeves per KT, arranged in parallel. The sleeves are linked to the KT through springs (elastic bonds). In this way, the poleward movement of a sleeve with respect to its MT requires the detachment and rebinding of all bonds, setting a large energy barrier for the movement at high sleeve insertion depths. This mechanism effectively prevents the poleward movement of a sleeve (and hence its KT) when the MT is in polymerization state, which leads to deeper insertion of the MT into the sleeve, while favoring the poleward movement of a sleeve (and hence its KT) when the MT is in a depolymerization state, which reduces the insertion depth. Thus, in the Joglekar-Hunt model, the primary factor driving P and AP KT movement is MT dynamics. In contrast, individual KT–MT bonds (Ndc80 complexes) are independent from one another in our model, and although the primary factor driving the P movement is poleward flux by pulling on the MT-bound Ndc80 complexes, the depolymerization rate of kMT plus ends is governed by the dynamics of the bonds, which in turn are regulated by tension forces. Like Joglekar and Hunt (2002), we assume that the bonds have a high affinity for the MT, but in our model, these bonds detach in a force-sensitive manner, with different kinetics, from polymerizing and depolymerizing MT tips, and independently from one another. Specifically, we assume that when a bond is under moderate levels of tension, detachment is favored from a polymerizing MT tip, and suppressed from a depolymerizing MT tip (prolonging the bond half-life on depolymerizing MTs), but at high levels of tension, detachment is also favored from a depolymerizing MT tip (Akiyoshi et al., 2010). Consequently, in contrast with what is observed in the Joglekar-Hunt model, in our model bonds with a polymerizing MT are generally "weak," and those with a depolymerizing MT are generally "strong." In addition, we assume that the tension exerted on an MT tip by the KT–MT bonds is sufficient to alter MT plus end dynamics to account for the slip-clutch mechanism proposed by others (Maddox et al., 2003).

Other FB models have also been developed to account for the metaphase chromosome behavior in *Drosophila* or fission yeast (Civelekoglu-Scholey et al., 2006; Courtheoux et al., 2009; Gay et al., 2012). The FB model developed by Courtheoux et al. (2009) addresses the correction of merotelic attachments in fission yeast during anaphase and does not account for amphitelic KT pairs. This model is derived from a previous model (Civelekoglu-Scholey et al., 2006) with additional and significant simplifying assumptions. Similarly to the model by Courtheoux et al. (2009), another quantitative model, recently developed by the Tournier group to account for the dynamics of amphitelic KT pairs in fission yeast (Gay et al., 2012), relies upon a macroscopic approach. There too, all KT components are represented by a homogeneous viscoelastic "unit" that can attach/detach from MTs, and neither individual MTs' plus-end positions and dynamics nor the reciprocal effect of the KT and the MT plus end dynamics on the attachment to/detachment from the KT are considered. Furthermore, because individual MTs are not accounted for, an MT is assumed to instantly switch to polymerization or depolymerization and to follow the direction of the KT upon attachment. Therefore, the questions that form the basis of our study—namely (a) how are the growth/shrinkage state and rate of different MTs attached to each KT coordinated, and (b) how is the movement of the sister KTs coordinated to give rise to the observed movements of sister KT pairs—are not and cannot be addressed in the framework proposed by Gay et al. (2012).

The framework of the FB model developed for the fast mitosis of the *Drosophila* embryo (Civelekoglu-Scholey et al.,

2006) forms the basis of the model presented here. This primary model, which relied on a major role of the two antagonistic KT motors dynein and CENP-E, and the two members of the kinesin-10 family MT depolymerases located at the KTs and at the spindle poles, can be adapted to account for many aspects of the metaphase chromosome dynamics in PtK1 cells, specifically by incorporating force-sensitive detachment rates for the KT motors dynein and CENP-E. However, the experimental test of this model's predictions on the observed dichotomy in the behavior of middle and peripheral KTs in PtK1 cells fails to validate the model and its central assumption that motors drive metaphase chromosome dynamics in PtK1 cells. In addition, with this model, we could not identify a set of parameters that could account for the observed period doubling of inter-KT stretch (Wan et al., 2012). This suggests that the KT motors dynein and CENP-E may be functioning as a back-up (error correction) or fine-tuning mechanism for the KT–MT attachment enabled by nonmotor linkages that drive the metaphase chromosome dynamics in PtK1 cells, and underscores how even highly conserved molecular mechanisms may be differentially deployed in different organisms.

The importance of understanding KT dynamics

The model developed in this study incorporates important emerging features of the eukaryotic KT and recapitulates the complex dynamic behavior of metaphase chromosomes in PtK1 cells. As such, this model can be extended to account for chromosome behavior in other cell types by altering specific parameters and adding forces resulting from plus and/or minus end–directed motors at the KT to the core model equations. Moreover, this model can be used to investigate the behavior and dynamics of misattached KTs. Finally, the work presented here sets the quantitative framework to investigate the role of various mechanisms, such as the gradient of centromeric Aurora B, the dynamics of Ndc80 attachment and detachment, the MT plus end dynamics, and the MT poleward sliding forces, proposed to contribute to correction of KT misattachments (Ganem et al., 2005; Cimini et al., 2006; DeLuca et al., 2006). Indeed, whereas chromosome oscillations are not absolutely required for the execution of mitosis, as several cell types that do not display chromosome oscillations can successfully segregate their chromosomes, the dynamics of oscillation or lack thereof inform us on the dynamics of KT–MT interactions, which play a key role in the correction of KT misattachments. Thus, the model developed here will be invaluable in helping us understand the correction mechanisms of KT misattachment that are essential to prevent chromosome missegregation and aneuploidy.

Materials and methods

Experimental methods

Generation of HEC1-GFP PtK1 cell line. A PtK1 cell line stably expressing the human HEC1 gene fused in frame with the EGFP was produced through the transduction of retroviral particles according to the instructions for high-titer retrovirus production provided by Takara Bio Inc. The EGFP-N1 plasmid carrying the *HEC1* gene was a gift from J. DeLuca (Colorado State University, Fort Collins, CO). In brief, the *HEC1-EGFP* gene was initially subcloned into the XhoI and NotI sites of the pLNCX2 retroviral vector (Takara Bio Inc.) that harbors the Ψ packaging sequence. To produce high-efficiency retroviral particles, we transfected the packaging GP2-293 cells (Takara Bio Inc.), carrying the viral *gag* and *pol* genes, with the pLNCX2-*HEC1-EGFP* plasmid together with the VSV-G vector (Takara Bio Inc.) that provided the viral envelope gene (*env*). The resulting retroviral particles were used to infect PtK1 cells that were subsequently placed under selection in Geneticin-containing media to obtain the final HEC1-GFP PtK1 cell line used in this study.

Cell culture. PtK1 and HEC1-GFP PtK1 cells were grown in HAM's F-12 media (Invitrogen) supplemented with 5% sodium pyruvate (Invitrogen), 1% antibiotic-antimycotic (Invitrogen), and 10% fetal bovine serum (Invitrogen), and maintained at 37°C in a humidified CO_2 incubator. For experiments, cells were grown on sterilized acid-washed coverslips inside 35-mm Petri dishes for 48 h before fixation/observation.

Immunostaining. For Hec1/anti-centromere antigen (ACA)/α-tubulin staining, cells were prefixed in freshly prepared 4% formaldehyde for 5 s before a 5-min lysis in 0.5% Triton X-100 in PHEM buffer (60 mM Pipes, 25 mM Hepes, 10 mM EGTA, and 2 mM $MgSO_4$, pH 7.0) and a 20-min fixation in 4% formaldehyde. For CENP-E and dynein staining, cells were briefly rinsed in PBS, fixed in freshly prepared 4% formaldehyde for 20 min, and then permeabilized with 0.1% Triton X-100 in PHEM buffer for 10 min. A 1-h block in 10% boiled goat serum (BGS) at room temperature was followed by overnight incubation with primary antibodies diluted in 5% BGS in PHEM buffer at 4°C. Cells were then washed four times in PBS with 0.1% Tween 20 (PBST), incubated with secondary antibodies for 45 min, washed in PBST, stained with DAPI, and mounted on microscope slides with an anti-fading solution containing 90% glycerol, 10% Tris buffer, and 0.5–1% *n*-propyl gallate. Primary antibodies were diluted as follows: human ACA (Antibodies Inc.), 1:100; mouse anti-Hec1 (Abcam), 1:500; rabbit anti-tubulin (Abcam), 1:200; rabbit anti–CENP-E (a gift of T. Yen, Fox Chase Cancer Center, Philadelphia, PA), 1:200; and mouse anti–dynein-IC (Sigma-Aldrich), 1:100. Secondary antibodies were diluted as follows: Red-X-goat anti–human (Jackson ImmunoResearch Laboratories, Inc.), 1:100; Cy5 goat anti–rabbit (Invitrogen), 1:100; and Alexa Fluor 488 goat anti–mouse (Invitrogen), 1:200.

Microinjection. Kif2a antibodies were purified by IgG affinity purification (Nab Spin kit; Thermo Fisher Scientific) from rabbit anti-Kif2a total serum (a gift of D. Compton, Geisel School of Medicine at Dartmouth, Hanover, NH). For microinjection, both Kif2a and Hec1 9G3 (Abcam) antibodies were dialyzed and concentrated into HEK buffer (20 mM Hepes, 100 mM KCl, and 1 mM DTT, pH 7.7) to a final concentration of 1.45 mg/ml. Cells were injected with HEK buffer alone (controls), Kif2a, or Hec1 9G3 antibody solution diluted 1:1 in HEK buffer (Kif2a alone or Hec1 alone), or a 1:1 mixture of Kif2a and Hec1 9G3 antibodies (Kif2a + Hec1 antibody coinjection). For microinjection, coverslips with HEC1-GFP PtK1 cells were mounted into modified Rose chambers (Rieder and Hard, 1990) without the top coverslip and incubated at 37°C with Phenol red–free L-15 media (Gibco) complemented with 4.5 g/liter glucose and covered with mineral oil to prevent evaporation. A volume corresponding to ~5% of the cell volume was injected into late prometaphase/early metaphase cells using a micromanipulator (NT-88-V3; Narishige) and a microinjection system (PLI-100A; Harvard Apparatus).

Microscopy and image acquisition. For inter- and intra-KT stretching analysis, immunostained cells were imaged with a swept field confocal unit (Prairie Technologies) attached to a microscope (Eclipse TE2000-U; Nikon). For CENP-E and dynein fluorescence intensity quantification, immunostained cells were imaged with an inverted microscope (Eclipse Ti; Nikon) with a Lumen 200PRO fluorescence illumination system (Prior Scientific). This latter setup was also used for live-cell imaging of microinjected cells. Both microscopes were equipped with motorized stages (Prior Scientific), and on both microscopes images were obtained with an HQ2 charge-coupled device camera (Photometrics), using a 100×/1.4 NA Plan-Apochromatic phase-contrast objective lens. Digital images were acquired using the NIS Elements software (Nikon). For fixed cells, z-series stacks were obtained at 0.6-µm steps. A dataset obtained during a previous study (Cimini et al., 2004) was used for initial characterization of chromosome dynamics (Fig. 1, B–F). For the microinjection experiments described in Fig. 7, imaging began shortly after injection. Near-simultaneous phase contrast and single focal plane epifluorescence images were acquired every 20 s for at least 11 min.

Image analysis. For each cell, measurements were taken on four pairs of sister KTs. Two pairs closest to the spindle long axis were chosen as representative of the middle KT pairs (Fig. 1 A), whereas the two outermost pairs of sister KTs (one on each side of the spindle axis, at the periphery of the metaphase plate) represented the peripheral KT pairs

(Fig. 1 A). To measure the inter- and intra-KT distances, fluorescence intensity profiles for the ACA and Hec1 signals were generated automatically by the NIS Elements software. The inter-KT distance was measured as the distance between the two centroids of the X-rhodamine–labeled ACA within a sister KT pair (Fig. 2 B). The intra-KT distance was measured as the distance between the centroids of the X-rhodamine–labeled ACA and the Alexa Fluor 488–labeled Hec1 fluorescent signals within a single KT (Fig. 2 C). KT fluorescence intensity of various antigens was measured with ImageJ using a method adapted from Hoffman et al. (2001). Two circles with diameter of 1.12 µm and 1.47 µm (with area A_{inner} and A_{outer}) were centered over each KT on an appropriate focal plane, and the integrated intensity was measured for each circle and as F_{inner} and F_{outer}. The mean background fluorescence (F_{meanbg}) was represented by the mean fluorescence in the ring area between the two circles: $F_{meanbg} = (F_{outer} - F_{inner})/(A_{outer} - A_{inner})$. The total fluorescence intensity of the protein is: $F = (F_{inner}/A_{inner} - F_{meanbg}) \times A_{inner}$. The total fluorescence intensity for the motor protein of interest was represented as a fraction of the ACA fluorescence intensity at the same KT.

KT tracking. Two middle and two peripheral KT pairs (Fig. 1 A) were tracked for each time-lapse video. Alexa Fluor 488 anti–CENP-F signals (Fig. 1, B–F) were tracked automatically using a previously developed MATLAB (MathWorks) program (Wan et al., 2012). HEC1-GFP signals were tracked manually aided by the same MATLAB program (Wan et al., 2012). KT position was defined as the Alexa Fluor 488/GFP signal centroid based on a 2D Gaussian fitting method (Wan et al., 2012).

Modeling methods

In all descriptions of the modeling methods, the sister chromatids' behavior is described along the pole–pole axis of the spindle, in one dimension. The positions of the KT and the MT plus and minus ends correspond to distances from the spindle equator, located at the origin ($x = 0$), and the positions of the left and right spindle poles are $x = -6.5$ and $x = 6.5$ µm, respectively, mimicking the metaphase steady-state spindle length of ~13 µm in PtK1 cells. All forces and velocities associated with the right and left KTs and kMTs are assumed to be positive in the poleward direction (toward the right pole for the KT tethered to the right pole, and toward the left pole for the KT tethered to the left pole). The time-dependent position of the right and left sister KTs (X^R_{KT} and X^L_{KT}), the right and left KT attached ith kMT's plus end ($x^R_{kMT,i}$ and $x^L_{kMT,i}$), and the pole proximal end of the right and left sister KT's ith kMT's kth Ndc80 complex ($x^{R_{i,k}}_{Ndc80}$ and $x^{L_{i,k}}_{Ndc80}$) are all measured with respect to the spindle equator (Fig. 4, A–C). The time-dependent velocities of the right and left sister KTs, and the poleward sliding/flux velocity of the ith kMT attached to the right and left sister KT, are: v^R_{chr}, v^L_{chr}, $v^R_{kMT,i}$, and $v^L_{kMT,i}$, respectively (Fig. 4 C).

In our models, we make the following simplifying assumptions:

(a) The motility events examined here are exclusively driven by an intrinsic balance of forces generated in the spindle.

(b) Throughout metaphase, spindle length (pole–pole distance) is maintained by a balance of antagonistic forces generated at antiparallel overlapping interpolar MTs and by astral MTs. In this model, as in previous considerations of KT positioning (Joglekar and Hunt, 2002; Civelekoglu-Scholey et al., 2006), we do not address how changes in spindle pole positions can/may affect KT positions and vice versa.

(c) All motor protein/nonmotor linkage (Ndc80 complex)-generated forces at the KTs or on the MTs are additive. For motor proteins, the total force depends linearly on the total number of attached/active force generators (i.e., motors share the load equally). For nonmotor linkages (Ndc80 complexes), the force exerted on the MT and the KT by each molecule is proportional to its tension/compression. We assume that all motor enzymes considered have linear force-velocity relationships, and the attachment/detachment kinetics of each motor in response to applied force is considered explicitly in a Monte-Carlo approach in the current models (Coppin et al., 1997; Svoboda and Block, 1994; Valentine et al., 2006).

(d) Active MT depolymerases (kinesin-13) located at the spindle poles depolymerize the kMT minus ends at the same rate at which MTs slide into the poles through the action of sliding motors, and additional poleward pulling forces which may result from the depolymerization activity of depolymerases are not accounted for.

Model framework. Both models consist of a large set of coupled FB equations describing the poleward and anti-poleward forces exerted on the left and right sister KTs, and on each kMT attached to the left and right sister KT (Fig. 4, A and D). The forces accounted for in the models are:

(a) For each sister KT: (1) cohesin-generated forces (AP directed); (2) sum of forces generated by attached and active KT motors (or Ndc80 complexes) at the KT (P or AP directed); (3) PEFs (AP or P directed); (4) polymerization ratcheting forces generated by kMT plus ends which impinge on the inner KT plate (AP directed; only accounted for in the KT-motor model); and (5) viscous drag forces on the chromosome (P or AP directed).

(b) For each kMT attached to a KT: (1) sum of poleward sliding motor–generated forces (P directed); (2) sum of the kMT-attached and active KT motor (or kMT-attached Ndc80 complex)-generated forces (AP or P directed); and (3) polymerization ratcheting forces generated by the kMT plus end when it impinges on the inner KT plate (P directed; only accounted for in the KT-motor model). We neglect the viscous drag forces on the kMT (Howard, 2001).

(c) MTs not attached to the KT but within the k-fiber are assumed to flux poleward by sliding and depolymerization at the mean sliding rate of the kMTs of the k-fiber.

Because the velocities of the KTs and the kMTs (i.e., the time-derivatives of their position $dX^R_{KT}/dt = v^R_{chr}$, $dX^L_{KT}/dt = v^L_{chr}$, $dX^{R,i}_{kMT}/dt = v^{R,i}_{sliding}$, and $dX^{L,i}_{kMT}/dt = v^{L,i}_{sliding}$), are determined by the forces acting on them at any given time, the solution to the large set of coupled ordinary differential equations (ODEs) formed as described in a–c yields the dynamics of the sister KTs and the kMTs over time. In this system of ODEs, the two equations for the sister KTs are coupled through the cohesin forces proportional to $X^R_{KT} - X^L_{KT}$, whereas the equations for the left and right sister KTs' kMTs are coupled to one another via the velocity of their respective KT.

Sliding motor/dynein/CENP-E force–velocity relationship and force-dependent detachment rates. In both models considered here, similarly to Civelekoglu-Scholey et al. (2006), we assume that the motor proteins (dynein, CENP-E, and sliding motors, as it applies) have a linear force–velocity relationship (Valentine et al., 2006), described by

$$F(v) = F_{stall}\left(1 - \frac{v}{V^{max}_{sliding}}\right),$$

where v is the time-dependent velocity of the motor on its MT track. In addition, we assume that the motors detach from the MTs in a force-dependent manner, described by

$$k^{motor}_{off}(f) = k^{motor}_{off}(0)\exp\left(\frac{f}{F^{motor}_{det}}\right),$$

where $k^{motor}_{off}(0)$ and F^{motor}_{det} are the detachment rate in the absence of load, and the force at which the detachment rate increases e-fold, respectively.

MT plus and minus end dynamics. As in Civelekoglu-Scholey et al. (2006), we assume that the plus ends of kMTs undergo DI, whereas the minus ends are depolymerized by the combined action of poleward sliding and depolymerization (Mitchison and Kirschner, 1984; Mitchison, 1989; Rogers et al., 2004). The DI of the MT plus ends is characterized by four parameters: v_g, v_s, f_{cat}, and f_{res} (Verde et al., 1992). We assume that the MTs' growth (polymerization) and shrinkage (depolymerization) rates are hindered by a factor k_{vg} and k_{vs} when the MT tip penetrates into the outer KT. The "boundary/edge" position of the outer KT is defined differently in the motor protein– and nonmotor linkage–based models considered here. In the motor protein–based model, where dynein and CENP-E are considered, the "edge" of the KT is set at 0.2 µm in the poleward direction (intra-KT distance) from the position of the inner KT-plate, and this intra-KT distance is constant over time. In the viscoelastic linkage-based model, where Ndc80 complexes provide the sole link between the KT and the MTs, the position of the outer KT edge for each sister KT is defined as the current position of their most stretched Ndc80 complex's attachment site to the kMT (Fig. 4 C). Among the DI rates, the catastrophe and rescue frequencies of the plus ends of MTs that are not attached to the KTs are defined by f^0_{cat} and f^0_{res}, respectively. For kMTs, however, these frequencies are assumed to be regulated differently in the two models considered here, and are explained in the following sections in each case.

Distribution of PEFs. Recent studies identified the distribution of the PEFs in PtK1 cells (Ke et al., 2009). Based on these studies, we assume a constant PEF from the spindle pole to a predefined point, x_d, within the half spindle, and a linearly decreasing function within the interval $[-x_d, x_d]$, as shown in Fig. 6 A (black line). Thus, the distribution of the PEFs in the models described in the following sections differs from our and others' previous consideration (Joglekar and Hunt, 2002; Civelekoglu-Scholey et al., 2006).

Numerical solution method and algorithm Here we outline the general methods of solution of the system of ODEs (typically composed of 52–102 equations) for both models, and further model-specific details are described separately in subsequent sections. The large set of coupled ODEs obtained by writing the FB equations on the sister KTs and their kMTs are solved with a forward Euler algorithm as described in Civelekoglu-Scholey et al. (2006) using custom-made MATLAB scripts. In the script, the initial conditions are as follows: sister KTs are positioned around the equator ($x = 0$), at rest length (d_0^{coh}) away from one another. The MT plus ends are randomly positioned near the KTs (using the built-in uniform pseudorandom number generator in MATLAB, *rand*), and all MT minus ends are positioned at the spindle poles. The polymerization/depolymerization state of the MT plus ends are selected randomly (*rand*), and all motor proteins (sliding, CENP-E, and dynein, as it applies) and nonmotor linkages (Ndc80 complexes, as it applies) are initially "free," not attached to MTs. In the new model, at $t = t_0$, all Ndc80 complexes (viscoelastic bonds) are at rest, with their pole-proximal end located at rest length (d_0^{Ndc}) distance away from their KT. Thus, the system is at rest, and no kMT or motor protein–Ndc80 complex is attached, hence all forces are equal to zero except for the PEFs (equal in magnitude, opposite in direction) at the current positions of the sister KTs.

Starting from these initial conditions (which differ slightly from one another at each realization due to the pseudorandom number generator used for the MT plus ends), at each time step t_n ($t_{n+1} = t_n + \Delta t$) in the algorithm, we begin by executing the attachment/detachment event of each motor protein (and/or each Ndc80 complex) by computing the probability of its attachment/detachment kinetic under the current load. To this end, first, the attachment/detachment rates (k_{on} or k_{off}) of the motor proteins/Ndc80 complexes are computed. If a kinetic rate is force-dependent, for example, for $k = k_{off}(f)$, the current rate is determined using the current force on the protein, via $k_{off}(f) = k_{off}^0 \exp(f / F_{det})$, where k_{off}^0 and F_{det} are the detachment rate at zero load and the force at which detachment rate decreases e-fold, respectively (Fig. S1 A). Then, for each motor, the probability of detachment/attachment is computed using $P = 1 - \exp(-k)$, where k represents the appropriate kinetic rate. Next, a pseudorandom number, r, is selected for each motor using the MATLAB function *rand*. If $r < P$, the event (attachment/detachment) is realized, and the current state of the motor protein–Ndc80 complex is updated to "attached" from "free," or vice versa. If $r \geq P$, the state of the motor protein–Ndc80 complex is left unchanged. Once the attachment/detachment events are executed, the set of FB equations (algebraic) are solved using the updated number of attached motor protein–Ndc80 complexes at the current time step, yielding the velocities of and forces exerted on the kMTs, motors, and sister KTs. Next, the stochastic switch rate of each MT plus end is computed similarly to the attachment/detachment of motor protein–Ndc80 complex as described in the beginning of this paragraph. We assume that $P = 1 - \exp(-f_{cat})$ (or $P = 1 - \exp(-f_{res})$) is the probability of catastrophe (or rescue) of a MT plus end, and this probability is compared with a random number, r, as described earlier in this paragraph to execute the switch between the growth and shrinkage state of each MT plus end. Finally, once the states of all MT plus ends are determined, the position of each sister KT is updated using its newly computed velocity v_{chr}, as $X_{KT}^R(t_{n+1}) = X_{KT}^R(t_n) + v_{chr}^R \Delta t$, whereas each MT plus end is moved poleward using its newly computed sliding rate $v_{sliding}$, and its newly computed polymerization/depolymerization state $v_{poly/depoly}^{R,i}(t)$, as $X_{kMT}^{R,i}(t_{n+1}) = X_{kMT}^{R,i}(t_n) + v_{sliding}^{R,i} \Delta t + v_{poly/depoly}^{R,i}$. Also, the force on each motor protein–Ndc80 complex is updated with the newly computed force, to be used for the stochastic kinetic computation in the next time step. The time step is incremented, and the sequence of events are repeated typically for thousands of time steps, equivalent to several hours in real time, to ensure stable behaviour.

FB model adapted from the model for *Drosophila* embryo: rescue and catastrophe frequency of kMT plus ends. In this model, the kMT plus end DI is the same as in Civelekoglu-Scholey et al. (2006). Namely, we assume that depolymerases (kinesin-13) located at the KT alter the rescue frequency of kMTs in a tension-dependent manner. We assume that the depolymerase effectively acts on the plus ends of the MTs when tension is low, and its action is diminished with tension. The tension on the kMT is $F_{tension} = (\alpha F_{cohesin} + \beta F_{PE} + \gamma F_{KT})/M$, (see Fig. 4 A for forces), where M is the current number of attached MTs to the KT in consideration (left or right), and α, β, and γ are nondimensionalization factors (units of pN^{-1}). Then tension dependence of rescue frequency is defined by:

$$f_{res}(F_{tension}) = f_{res}^0 \exp\left(-\frac{F_{tension}}{F_{res}}\right),$$

where f_{res}^0 and F_{res} are the tension-free rescue frequency and the tension force at which the effect of the KT-associated depolymerase decreases by e-fold, respectively (Sprague et al., 2003). When the MT plus end contacts and begins impinging on the KT plate, we assume that it stops growing (adding tubulin subunits to its plus end) and its catastrophe frequency is increased by a factor of φ (i.e., $f_{cat}^{impinge} = f_{cat} / \varphi$), and its rescue frequency returns to low tension state f_{res}^0, regardless of the current tension on the KT, while it continues to impinge on the KT plate.

FB model for PtK1 cell chromosome dynamics: viscoelastic KT–MT linkages in the absence of KT-motors. The framework of this model is identical to the model described in the previous section. However, the molecules responsible for forces on the KT and the kMT and their biophysical properties differ. Specifically, here we assume that force resulting from the opposing action of active CENP-E and dynein motors at the KT is of negligible magnitude during metaphase, and we do not account for these forces. Instead, we assume that the nonmotor viscoelastic linkages (Ndc80 complexes) provide the attachment of the sister KTs to spindle MTs, and the stretching/compression of these Ndc80 complexes resulting from the relative movement of a KT and the kMT each complex is attached to, exerts a force on the KT and the kMT (Fig. S2 A). The forces exerted on the KTs (and the kMTs) by attached viscoelastic Ndc80 complexes are described by an elastic spring constant κ_{Ndc80}, and a viscous friction coefficient ε_{Ndc80} (Fig. 4 C and Table S1). We assume that when a kMT plus end reaches a critical distance from the KT plate, polymerization is hindered, and hence in this model we neglect polymerization ratcheting forces that may result from kMT plus ends impinging on the KT plate (i.e., $F_{poly} = 0$). Therefore, the equations for the KTs and the kMTs in Civelekoglu-Scholey et al. (2006) were further revised by eliminating the motor-generated forces and replacing them by the Ndc80 complex–generated forces, as well as by eliminating the polymerization ratcheting forces ($F_{poly} = 0$; Fig. 4 D).

Force-dependent binding/detachment kinetics of the Ndc80 complex. In the model, we assume that the Ndc80 complexes exhibit the same attachment rates to, but different force-sensitive detachment rates from, polymerizing and depolymerizing MT ends. The pseudo first order attachment rate k_{on}^{Ndc80} (s^{-1}) is assumed to be independent of load, but the detachment rate k_{off}^{Ndc80} is assumed to be force dependent, and further assumed to be different for polymerizing and depolymerizing MTs in its functional form. The detachment rate of the Ndc80 complex from polymerizing MTs is assumed to increase exponentially with force, and is defined by

$$k_{off,poly}^{Ndc80}(f) = k_{off,poly}^{Ndc80}(0) \exp\left(\frac{f}{F_{poly}^{Ndc}}\right),$$

where $k_{off,poly}^{Ndc80}(0)$ is the detachment rate in the absence of load, and F_{poly}^{Ndc} is the critical load force at which the rate increases e-fold (Fig. S2 B). The force dependence of the detachment rate of Ndc80 complex from depolymerizing MTs, however, is assumed to have a biphasic shape: it initially decreases in response to force, then increases under larger forces. In the model, it is described by

$$k_{off,depoly}^{Ndc80}(f) = k_{off,depoly}^{Ndc80}(0) \exp\left(\frac{f}{F_{depoly}^{Ndc}}\right) \exp\left(\frac{f - F_{switch}}{F_{depoly}^{Ndc}}\right),$$

where $k_{off,depoly}^{Ndc80}(0)$ is the detachment rate in the absence of load, F_{depoly}^{Ndc} is the critical load force at which the rate decreases e-fold, and F_{switch} is the load force typical of the turnaround in detachment rate (Fig. S2 C). This type of biphasic (catch-bond) behavior is typical of adhesion molecules (Dembo et al., 1988; Evans, 2001), but is not a characteristic property of MT-based motors, including kinesins and dynein (Coppin et al., 1997; Toba et al., 2006; Valentine et al., 2006).

MT plus and minus end dynamics. We assume that the MT plus end polymerization/growth rate is limited by the position of the KTs, and that MTs cannot grow into or past the inner KT. We also assume that a KT-attached MT (a kMT) cannot depolymerize past the position of an attached Ndc80 complex; i.e., a tubulin dimer to which an Ndc80 complex is attached cannot be dissociated from the lattice. Consequently, the depolymerization/shrinkage rate of each kMT is limited by the position of the attachment point of its Ndc80 complex closest to its KT. We assume that the rescue frequency of MT plus ends depends on tension force, F, on the kMT, increasing with tension $f_{res}(F) = f_{res}^0 \exp(F / F_{res})$, where f_{res}^0 and F_{res} are the rescue rate in the absence of load, and the tension force at which

rescue frequency increases e-fold, respectively. The catastrophe frequency of an MT plus end is assumed to be dependent on its growth velocity, and on its length (the effect of kinesin-8 motors, for example), increasing with a decreasing growth rate and increasing length (Janson et al., 2003; Varga et al., 2006). For an MT of length *l*, growing at rate *v*, the catastrophe frequency is therefore defined by

$$f_{cat}(l, v) = f_{cat}^{0}\left(\frac{l}{L_{av}}\right)\exp\left(\frac{V_{free} - v}{V_g}\right),$$

where f_{cat}^{0} is the catastrophe frequency for "free" growth rate ($V_{free} = v_g/k_{vg}$), V_g is the critical growth rate at which the catastrophe frequency decreases e-fold, L_{av} is the mean MT length in the spindle, and f_{cat}^{0} represents its catastrophe rate. For the plus ends of the unattached MTs, $v = V_{free} = v_g$.

Polar ejection forces. The PEF function is as described above ("Distribution of PEFs" section and Fig. 6 A). For the solutions shown in Fig. 5, the linearly decreasing PEF function shown in black in Fig. 6 A was used, and for the solutions shown in Fig. 6 (B–G), the nonlinear PEF function shown in red in Fig. 6 A was used. We propose that the PEF functions differ between the middle KTs and the peripheral KTs in two ways. First, PEFs have different baseline values (higher for the peripheral chromosomes) at positions proximal to the poles (Fig. 6 A). This difference in the baseline value is based on a simple and conservative approximation of the number of MTs nucleated at the pole that can potentially reach the chromosome arms as follows: assuming that the surface area of the chromosome arm can be approximated by an ellipse, with major axis length a_{middle} and $a_{peripheral}$, and same minor axis, the surface area of the peripheral and middle chromosome would obey $S_{peripheral} = (a_{middle}/a_{peripheral})^2 S_{middle}$. We conservatively assume that $a_{peripheral} = 3\ a_{middle}$. Further assuming that MT nucleation occurs only at the centrosomes equally in all directions, because the probability of MTs to encounter a chromosome arm is proportional to the surface area of the chromosome arm, this gives rise to the likelihood that an MT is $3^2 = 9$ times more likely to reach the arm of a peripheral chromosome at a distance proximal to the pole, where the length-dependent catastrophe rate of the MTs has little effect on MT plus end distribution (see explanation later in this paragraph), setting the baseline higher for the peripheral chromosomes. We propose that this is an underestimate, as there is also the additional "crowding" effect for the middle sister KTs, where they become shielded by neighboring chromosomes (as discussed in the results). Second, the PEFs increase linearly around the equator for the middle KTs and nonlinearly for the peripheral KTs (Fig. 6 A). For the middle chromosomes, it has been experimentally shown that PEFs increase in a sublinear fashion around the equator (Ke et al., 2009), and for simplicity, here we assume a linear distribution. A length-dependent catastrophe frequency of MT plus ends would give rise to a highly nonlinear distribution of MT plus ends at long distances, *x*, away from the poles, which is well described by $f_{PEF}(x) = \exp[-x\ln(x)]$ (Yadav and Mukherji, 2011). However, the experimental findings do not support such a nonlinear increase in PEFs for excursion distances displayed by middle sister KTs, roughly ranging from R/2 to 3R/2, where R is the half spindle length (Ke et al., 2009), suggesting that the PEFs remain within the linear regimen at this distance range. Nevertheless, because of the geometry of the spindle in these flat cells, the length of a MT impinging on the middle of a peripheral chromosome's arm (three times the size of one in the middle of the spindle), is on average twice as long as one in the middle of the spindle (differs approximately by a factor of $[\cos(\pi/3)]^{-1}$) at the same distance, *x*, away from the metaphase plate. Thus, here we propose that for the peripheral chromosome arms, the PEF function enters the nonlinear regimen, reflecting a length-dependent catastrophe rate of the MT plus ends.

Online supplemental material

Fig. S1 illustrates the features of the model with motor-dependent KT–MT interactions and the behavior of sister KTs within such model. Fig. S2 illustrates the forces exerted by Ndc80 complexes on a KT and its kMTs and the Ndc80 dissociation kinetics in the model based on nonmotor, viscoelastic bonds. Fig. S3 reports the model data for the distribution of the standard deviations of the distances from the pole for middle and peripheral KTs. Table S1 is a comprehensive list of the parameters used in our mathematical model. Video 1 shows computer simulations of KT and kMT dynamics for oscillating and nonoscillating sister KT pairs. Video 2 shows KT dynamics in HEC1-GFP PtK1 cells that were either uninjected or injected with Kif2a or Hec1 antibodies or a combination of the two. Online supplemental material is available at http://www.jcb.org/cgi/content/full/jcb.201301022/DC1.

We would like to thank all the members of the Cimini laboratory for useful discussion and helpful comments. We are also grateful to Tim Yen (Fox Chase Cancer Center, Philadelphia, PA) for providing the CENP-E antibody, Jennifer DeLuca (Colorado State University, Fort Collins, CO) for providing the HEC1-EGFP-N1 plasmid, and Duane Compton (Geisel School of Medicine at Dartmouth, Hanover, NH) for providing the rabbit anti-Kif2a total serum. We finally thank Alex Mogilner, Ted Salmon, Jon Scholey, and Jianhua Xing for critical reading of the manuscript, and Rob Gunter for technical assistance.

M. Shen was a recipient of an Institute for Critical Technology and Applied Science scholarship. This work was supported by National Science Foundation grant MCB-0842551 to D. Cimini and G. Civelekoglu-Scholey. Additional funding was provided by Human Frontier Science Program grant RGY0069/2010 to D. Cimini.

Submitted: 7 January 2013
Accepted: 11 April 2013

References

Akiyoshi, B., K.K. Sarangapani, A.F. Powers, C.R. Nelson, S.L. Reichow, H. Arellano-Santoyo, T. Gonen, J.A. Ranish, C.L. Asbury, and S. Biggins. 2010. Tension directly stabilizes reconstituted kinetochore-microtubule attachments. *Nature*. 468:576–579. http://dx.doi.org/10.1038/nature09594

Asbury, C.L., J.F. Tien, and T.N. Davis. 2011. Kinetochores' gripping feat: conformational wave or biased diffusion? *Trends Cell Biol.* 21:38–46. http://dx.doi.org/10.1016/j.tcb.2010.09.003

Bader, J.R., and K.T. Vaughan. 2010. Dynein at the kinetochore: timing, interactions and functions. *Semin. Cell Dev. Biol.* 21:269–275. http://dx.doi.org/10.1016/j.semcdb.2009.12.015

Brust-Mascher, I., and J.M. Scholey. 2002. Microtubule flux and sliding in mitotic spindles of *Drosophila* embryos. *Mol. Biol. Cell*. 13:3967–3975. http://dx.doi.org/10.1091/mbc.02-05-0069

Cameron, L.A., G. Yang, D. Cimini, J.C. Canman, O. Kisurina-Evgenieva, A. Khodjakov, G. Danuser, and E.D. Salmon. 2006. Kinesin 5-independent poleward flux of kinetochore microtubules in PtK1 cells. *J. Cell Biol.* 173:173–179. http://dx.doi.org/10.1083/jcb.200601075

Cheeseman, I.M., and A. Desai. 2008. Molecular architecture of the kinetochore-microtubule interface. *Nat. Rev. Mol. Cell Biol.* 9:33–46. http://dx.doi.org/10.1038/nrm2310

Cheeseman, I.M., J.S. Chappie, E.M. Wilson-Kubalek, and A. Desai. 2006. The conserved KMN network constitutes the core microtubule-binding site of the kinetochore. *Cell*. 127:983–997. http://dx.doi.org/10.1016/j.cell.2006.09.039

Cimini, D. 2008. Merotelic kinetochore orientation, aneuploidy, and cancer. *Biochim. Biophys. Acta*. 1786:32–40.

Cimini, D., L.A. Cameron, and E.D. Salmon. 2004. Anaphase spindle mechanics prevent mis-segregation of merotelically oriented chromosomes. *Curr. Biol.* 14:2149–2155. http://dx.doi.org/10.1016/j.cub.2004.11.029

Cimini, D., X. Wan, C.B. Hirel, and E.D. Salmon. 2006. Aurora kinase promotes turnover of kinetochore microtubules to reduce chromosome segregation errors. *Curr. Biol.* 16:1711–1718. http://dx.doi.org/10.1016/j.cub.2006.07.022

Civelekoglu-Scholey, G., D.J. Sharp, A. Mogilner, and J.M. Scholey. 2006. Model of chromosome motility in *Drosophila* embryos: adaptation of a general mechanism for rapid mitosis. *Biophys. J.* 90:3966–3982. http://dx.doi.org/10.1529/biophysj.105.078691

Coppin, C.M., D.W. Pierce, L. Hsu, and R.D. Vale. 1997. The load dependence of kinesin's mechanical cycle. *Proc. Natl. Acad. Sci. USA*. 94:8539–8544. http://dx.doi.org/10.1073/pnas.94.16.8539

Courtheoux, T., G. Gay, Y. Gachet, and S. Tournier. 2009. Ase1/Prc1-dependent spindle elongation corrects merotely during anaphase in fission yeast. *J. Cell Biol.* 187:399–412. http://dx.doi.org/10.1083/jcb.200902093

de Lartigue, J., I. Brust-Mascher, and J.M. Scholey. 2011. Anaphase B spindle dynamics in *Drosophila* S2 cells: Comparison with embryo spindles. *Cell Div.* 6:8. http://dx.doi.org/10.1186/1747-1028-6-8

DeLuca, J.G., W.E. Gall, C. Ciferri, D. Cimini, A. Musacchio, and E.D. Salmon. 2006. Kinetochore microtubule dynamics and attachment stability are regulated by Hec1. *Cell*. 127:969–982. http://dx.doi.org/10.1016/j.cell.2006.09.047

Dembo, M., D.C. Torney, K. Saxman, and D. Hammer. 1988. The reaction-limited kinetics of membrane-to-surface adhesion and detachment. *Proc. R. Soc. Lond. B Biol. Sci.* 234:55–83. http://dx.doi.org/10.1098/rspb.1988.0038

Desai, A., P.S. Maddox, T.J. Mitchison, and E.D. Salmon. 1998. Anaphase A chromosome movement and poleward spindle microtubule flux occur at similar rates in Xenopus extract spindles. *J. Cell Biol.* 141:703–713. http://dx.doi.org/10.1083/jcb.141.3.703

Dumont, S., E.D. Salmon, and T.J. Mitchison. 2012. Deformations within moving kinetochores reveal different sites of active and passive force generation. *Science*. 337:355–358. http://dx.doi.org/10.1126/science.1221886

Evans, E. 2001. Probing the relation between force—lifetime—and chemistry in single molecular bonds. *Annu. Rev. Biophys. Biomol. Struct.* 30:105–128. http://dx.doi.org/10.1146/annurev.biophys.30.1.105

Funabiki, H., I. Hagan, S. Uzawa, and M. Yanagida. 1993. Cell cycle-dependent specific positioning and clustering of centromeres and telomeres in fission yeast. *J. Cell Biol.* 121:961–976. http://dx.doi.org/10.1083/jcb.121.5.961

Ganem, N.J., and D.A. Compton. 2006. Functional roles of poleward microtubule flux during mitosis. *Cell Cycle*. 5:481–485. http://dx.doi.org/10.4161/cc.5.5.2519

Ganem, N.J., K. Upton, and D.A. Compton. 2005. Efficient mitosis in human cells lacking poleward microtubule flux. *Curr. Biol.* 15:1827–1832. http://dx.doi.org/10.1016/j.cub.2005.08.065

Gardner, M.K., and D.J. Odde. 2006. Modeling of chromosome motility during mitosis. *Curr. Opin. Cell Biol.* 18:639–647. http://dx.doi.org/10.1016/j.ceb.2006.10.006

Gay, G., T. Courtheoux, C. Reyes, S. Tournier, and Y. Gachet. 2012. A stochastic model of kinetochore-microtubule attachment accurately describes fission yeast chromosome segregation. *J. Cell Biol.* 196:757–774. http://dx.doi.org/10.1083/jcb.201107124

Grishchuk, E.L., M.I. Molodtsov, F.I. Ataullakhanov, and J.R. McIntosh. 2005. Force production by disassembling microtubules. *Nature*. 438:384–388. http://dx.doi.org/10.1038/nature04132

Hill, T.L. 1985. Theoretical problems related to the attachment of microtubules to kinetochores. *Proc. Natl. Acad. Sci. USA*. 82:4404–4408. http://dx.doi.org/10.1073/pnas.82.13.4404

Hoffman, D.B., C.G. Pearson, T.J. Yen, B.J. Howell, and E.D. Salmon. 2001. Microtubule-dependent changes in assembly of microtubule motor proteins and mitotic spindle checkpoint proteins at PtK1 kinetochores. *Mol. Biol. Cell*. 12:1995–2009.

Howard, J. 2001. Mechanics of motor proteins and the cytoskeleton. Sinauer Associates, Sunderland, MA. 367 pp.

Janson, M.E., M.E. de Dood, and M. Dogterom. 2003. Dynamic instability of microtubules is regulated by force. *J. Cell Biol.* 161:1029–1034. http://dx.doi.org/10.1083/jcb.200301147

Jaqaman, K., E.M. King, A.C. Amaro, J.R. Winter, J.F. Dorn, H.L. Elliott, N. McHedlishvili, S.E. McClelland, I.M. Porter, M. Posch, et al. 2010. Kinetochore alignment within the metaphase plate is regulated by centromere stiffness and microtubule depolymerases. *J. Cell Biol.* 188:665–679. http://dx.doi.org/10.1083/jcb.200909005

Joglekar, A.P., and J.G. DeLuca. 2009. Chromosome segregation: Ndc80 can carry the load. *Curr. Biol.* 19:R404–R407. http://dx.doi.org/10.1016/j.cub.2009.04.014

Joglekar, A.P., and A.J. Hunt. 2002. A simple, mechanistic model for directional instability during mitotic chromosome movements. *Biophys. J.* 83:42–58. http://dx.doi.org/10.1016/S0006-3495(02)75148-5

Ke, K., J. Cheng, and A.J. Hunt. 2009. The distribution of polar ejection forces determines the amplitude of chromosome directional instability. *Curr. Biol.* 19:807–815. http://dx.doi.org/10.1016/j.cub.2009.04.036

LaFountain, J.R. Jr., R. Oldenbourg, R.W. Cole, and C.L. Rieder. 2001. Microtubule flux mediates poleward motion of acentric chromosome fragments during meiosis in insect spermatocytes. *Mol. Biol. Cell*. 12:4054–4065.

Maddox, P., A. Desai, K. Oegema, T.J. Mitchison, and E.D. Salmon. 2002. Poleward microtubule flux is a major component of spindle dynamics and anaphase a in mitotic *Drosophila* embryos. *Curr. Biol.* 12:1670–1674. http://dx.doi.org/10.1016/S0960-9822(02)01183-1

Maddox, P., A. Straight, P. Coughlin, T.J. Mitchison, and E.D. Salmon. 2003. Direct observation of microtubule dynamics at kinetochores in *Xenopus* extract spindles: implications for spindle mechanics. *J. Cell Biol.* 162:377–382. http://dx.doi.org/10.1083/jcb.200301088

Magidson, V., C.B. O'Connell, J. Lončarek, R. Paul, A. Mogilner, and A. Khodjakov. 2011. The spatial arrangement of chromosomes during prometaphase facilitates spindle assembly. *Cell*. 146:555–567. http://dx.doi.org/10.1016/j.cell.2011.07.012

Maiato, H., J. DeLuca, E.D. Salmon, and W.C. Earnshaw. 2004. The dynamic kinetochore-microtubule interface. *J. Cell Sci.* 117:5461–5477. http://dx.doi.org/10.1242/jcs.01536

Maresca, T.J., and E.D. Salmon. 2009. Intrakinetochore stretch is associated with changes in kinetochore phosphorylation and spindle assembly checkpoint activity. *J. Cell Biol.* 184:373–381. http://dx.doi.org/10.1083/jcb.200808130

McIntosh, J.R., E.L. Grishchuk, and R.R. West. 2002. Chromosome-microtubule interactions during mitosis. *Annu. Rev. Cell Dev. Biol.* 18:193–219. http://dx.doi.org/10.1146/annurev.cellbio.18.032002.132412

McIntosh, J.R., E.L. Grishchuk, M.K. Morphew, A.K. Efremov, K. Zhudenkov, V.A. Volkov, I.M. Cheeseman, A. Desai, D.N. Mastronarde, and F.I. Ataullakhanov. 2008. Fibrils connect microtubule tips with kinetochores: a mechanism to couple tubulin dynamics to chromosome motion. *Cell*. 135:322–333. http://dx.doi.org/10.1016/j.cell.2008.08.038

Mitchison, T.J. 1989. Polewards microtubule flux in the mitotic spindle: evidence from photoactivation of fluorescence. *J. Cell Biol.* 109:637–652. http://dx.doi.org/10.1083/jcb.109.2.637

Mitchison, T., and M. Kirschner. 1984. Dynamic instability of microtubule growth. *Nature*. 312:237–242. http://dx.doi.org/10.1038/312237a0

Pearson, C.G., P.S. Maddox, E.D. Salmon, and K. Bloom. 2001. Budding yeast chromosome structure and dynamics during mitosis. *J. Cell Biol.* 152:1255–1266. http://dx.doi.org/10.1083/jcb.152.6.1255

Powers, A.F., A.D. Franck, D.R. Gestaut, J. Cooper, B. Gracyzk, R.R. Wei, L. Wordeman, T.N. Davis, and C.L. Asbury. 2009. The Ndc80 kinetochore complex forms load-bearing attachments to dynamic microtubule tips via biased diffusion. *Cell*. 136:865–875. http://dx.doi.org/10.1016/j.cell.2008.12.045

Rieder, C.L., and R. Hard. 1990. Newt lung epithelial cells: cultivation, use, and advantages for biomedical research. *Int. Rev. Cytol.* 122:153–220. http://dx.doi.org/10.1016/S0074-7696(08)61208-5

Rogers, G.C., S.L. Rogers, T.A. Schwimmer, S.C. Ems-McClung, C.E. Walczak, R.D. Vale, J.M. Scholey, and D.J. Sharp. 2004. Two mitotic kinesins cooperate to drive sister chromatid separation during anaphase. *Nature*. 427:364–370. http://dx.doi.org/10.1038/nature02256

Salic, A., J.C. Waters, and T.J. Mitchison. 2004. Vertebrate shugoshin links sister centromere cohesion and kinetochore microtubule stability in mitosis. *Cell*. 118:567–578. http://dx.doi.org/10.1016/j.cell.2004.08.016

Skibbens, R.V., V.P. Skeen, and E.D. Salmon. 1993. Directional instability of kinetochore motility during chromosome congression and segregation in mitotic newt lung cells: a push-pull mechanism. *J. Cell Biol.* 122:859–875. http://dx.doi.org/10.1083/jcb.122.4.859

Sprague, B.L., C.G. Pearson, P.S. Maddox, K.S. Bloom, E.D. Salmon, and D.J. Odde. 2003. Mechanisms of microtubule-based kinetochore positioning in the yeast metaphase spindle. *Biophys. J.* 84:3529–3546. http://dx.doi.org/10.1016/S0006-3495(03)75087-5

Stumpff, J., Y. Du, C.A. English, Z. Maliga, M. Wagenbach, C.L. Asbury, L. Wordeman, and R. Ohi. 2011. A tethering mechanism controls the processivity and kinetochore-microtubule plus-end enrichment of the kinesin-8 Kif18A. *Mol. Cell*. 43:764–775. http://dx.doi.org/10.1016/j.molcel.2011.07.022

Stumpff, J., M. Wagenbach, A. Franck, C.L. Asbury, and L. Wordeman. 2012. Kif18A and chromokinesins confine centromere movements via microtubule growth suppression and spatial control of kinetochore tension. *Dev. Cell*. 22:1017–1029. http://dx.doi.org/10.1016/j.devcel.2012.02.013

Svoboda, K., and S.M. Block. 1994. Force and velocity measured for single kinesin molecules. *Cell*. 77:773–784. http://dx.doi.org/10.1016/0092-8674(94)90060-4

Toba, S., T.M. Watanabe, L. Yamaguchi-Okimoto, Y.Y. Toyoshima, and H. Higuchi. 2006. Overlapping hand-over-hand mechanism of single molecular motility of cytoplasmic dynein. *Proc. Natl. Acad. Sci. USA*. 103:5741–5745. http://dx.doi.org/10.1073/pnas.0508511103

Torosantucci, L., M. De Santis Puzzonia, C. Cenciarelli, W. Rens, and F. Degrassi. 2009. Aneuploidy in mitosis of PtK1 cells is generated by random loss and nondisjunction of individual chromosomes. *J. Cell Sci.* 122:3455–3461. http://dx.doi.org/10.1242/jcs.047944

Uchida, K.S., K. Takagaki, K. Kumada, Y. Hirayama, T. Noda, and T. Hirota. 2009. Kinetochore stretching inactivates the spindle assembly checkpoint. *J. Cell Biol.* 184:383–390. http://dx.doi.org/10.1083/jcb.200811028

Valentine, M.T., P.M. Fordyce, T.C. Krzysiak, S.P. Gilbert, and S.M. Block. 2006. Individual dimers of the mitotic kinesin motor Eg5 step processively and support substantial loads in vitro. *Nat. Cell Biol.* 8:470–476. http://dx.doi.org/10.1038/ncb1394

VandenBeldt, K.J., R.M. Barnard, P.J. Hergert, X. Meng, H. Maiato, and B.F. McEwen. 2006. Kinetochores use a novel mechanism for coordinating the dynamics of individual microtubules. *Curr. Biol.* 16:1217–1223. http://dx.doi.org/10.1016/j.cub.2006.04.046

Varga, V., J. Helenius, K. Tanaka, A.A. Hyman, T.U. Tanaka, and J. Howard. 2006. Yeast kinesin-8 depolymerizes microtubules in a length-dependent manner. *Nat. Cell Biol.* 8:957–962. http://dx.doi.org/10.1038/ncb1462

Varga, V., C. Leduc, V. Bormuth, S. Diez, and J. Howard. 2009. Kinesin-8 motors act cooperatively to mediate length-dependent microtubule depolymerization. *Cell*. 138:1174–1183. http://dx.doi.org/10.1016/j.cell.2009.07.032

Verde, F., M. Dogterom, E. Stelzer, E. Karsenti, and S. Leibler. 1992. Control of microtubule dynamics and length by cyclin A- and cyclin B-dependent kinases in *Xenopus* egg extracts. *J. Cell Biol.* 118:1097–1108. http://dx.doi.org/10.1083/jcb.118.5.1097

Vladimirou, E., E. Harry, N. Burroughs, and A.D. McAinsh. 2011. Springs, clutches and motors: driving forward kinetochore mechanism by modelling. *Chromosome Res.* 19:409–421. http://dx.doi.org/10.1007/s10577-011-9191-x

Wan, X., D. Cimini, L.A. Cameron, and E.D. Salmon. 2012. The coupling between sister kinetochore directional instability and oscillations in centromere stretch in metaphase PtK1 cells. *Mol. Biol. Cell*. 23:1035–1046. http://dx.doi.org/10.1091/mbc.E11-09-0767

Yadav, V., and S. Mukherji. 2011. Length-dependent dynamics of microtubules. *Phys. Rev. E Stat. Nonlin. Soft Matter Phys.* 84:062902. http://dx.doi.org/10.1103/PhysRevE.84.062902